


 Cite this: *RSC Adv.*, 2020, 10, 17602

Development of novel *N*-(6-methanesulfonyl-benzothiazol-2-yl)-3-(4-substituted-piperazin-1-yl)-propionamides with cholinesterase inhibition, anti- β -amyloid aggregation, neuroprotection and cognition enhancing properties for the therapy of Alzheimer's disease†

 Chandra Bhushan Mishra,^{‡a} Shruti Shalini,^{‡a} Siddharth Gusain,^a Amresh Prakash,^{ID b} Jyoti Kumari,^a Shikha Kumari,^a Anita Kumari Yadav,^a Andrew M. Lynn^c and Manisha Tiwari^{ID *a}

A novel series of benzothiazole–piperazine hybrids were rationally designed, synthesized, and evaluated as multifunctional ligands against Alzheimer's disease (AD). The synthesized hybrid molecules illustrated modest to strong inhibition of acetylcholinesterase (AChE) and A β ₁₋₄₂ aggregation. Compound **12** emerged as the most potent hybrid molecule exhibiting balanced functions with effective, uncompetitive and selective inhibition against AChE (IC₅₀ = 2.31 μ M), good copper chelation, A β ₁₋₄₂ aggregation inhibition (53.30%) and disaggregation activities. Confocal laser scanning microscopy and TEM analysis also validate the A β fibril inhibition ability of this compound. Furthermore, this compound has also shown low toxicity and is capable of impeding loss of cell viability elicited by H₂O₂ neurotoxicity in SHSY-5Y cells. Notably, compound **12** significantly improved cognition and spatial memory against scopolamine-induced memory deficit in a mouse model. Hence, our results corroborate the multifunctional nature of novel hybrid molecule **12** against AD and it may be a suitable lead for further development as an effective therapeutic agent for therapy in the future.

Received 21st January 2020

Accepted 19th April 2020

DOI: 10.1039/d0ra00663g

rsc.li/rsc-advances

1. Introduction

Alzheimer's disease (AD) is a predominant source of irreversible dementia, resulting in more than 75% of the dementia cases worldwide. It is known to be a multifactorial neurodegenerative disorder designated by progressive loss of memory and other cognitive functions. The main risk factor of AD is aging; however the mechanism underlying the foundation of AD due to aging is yet to be firmly elucidated. It is clinically marked by the progression from episodic memory problems to a slow global decline of cognitive function. Patients in end-stage AD become bedridden and are highly dependent on custodial care,

with an average life span of 9 years after diagnosis.¹ AD leaves an enormous emotional and financial burden on patients, their families and society.

There are approximately 44 million people affected by Alzheimer's disease, and it is expected to increase three times by 2050; these perturbing numbers show that Alzheimer's disease (AD) remains a serious socio-economical problem.² AD is estimated to have cost the world \$604 billion in 2010 alone.³ These costs are staggering, particularly in light of worldwide increase in the number of AD cases. AD remains the most prevalent unmet medical need because of its chronicity, cost, severity, and lack of mechanism based treatment.⁴

Extensive research from several years has still not been able to establish the exact molecular-mechanistic aspects of AD. Clinically, AD is indicated by widespread neuronal cell death in the brain, which corresponds to deposition of abundant fibrillar plaques, primarily comprising the beta-amyloid (A β) peptide.^{5,6} The identified pathological hallmarks of AD are senile plaques of amyloid beta protein, intracellular neurofibrillary tangles (NFTs), and neuronal degeneration. Accumulation of A β peptides encourages conformational changes that lead to further non-covalent polymerization into a heterogeneous

^aDr. B. R. Ambedkar Centre for Biomedical Research, University of Delhi, New Delhi 110007, India. E-mail: mtiwari07@gmail.com

^bAmity Institute of Integrative Sciences and Health (AIISH), Amity University Haryana, Amity Education Valley, Gurgaon-122413, India

^cSchool of Computational & Integrative Sciences, Jawaharlal Nehru University, New Delhi 110067, India

† Electronic supplementary information (ESI) available: *In silico* study data, ¹H and ¹³C spectra of all synthesized compounds have been kept as supplementary data. See DOI: 10.1039/d0ra00663g

‡ These authors contributed equally to this work.



range of oligomeric class that finally forms amyloid fibrils.⁷ Vulnerability of brain to oxidative stress is due to its high demand for oxygen, abundant lipid content and relative scarcity of antioxidant enzymes.⁸⁻¹⁰ Consequences of neuronal loss because of oxidation include upregulation of proinflammatory cytokines and irreparable DNA damage.^{11,12} Metal dyshomeostasis in the body, especially in the brain, can be a critical mechanism for neurodegenerative processes, including oxidative stress generation or amyloid plaques aggregation.¹³

Despite the fact that Alzheimer's disease (AD) was first described over 100 years ago, disease-modifying treatment has not yet been developed for this disease. There is no complete cure for AD, but some medicines can ameliorate its clinical symptoms by having an impact on cognitive functions, delaying functional decline and improving behavioural changes.^{14,15} Still, their therapeutic interest is limited owing to their side effects and to the fact that they only treat symptoms. There are only four drugs in the market for the treatment of AD, three cholinesterase inhibitors (Donepezil, Rivastigmine, Galantamine) and an *N*-methyl-D-aspartate (NMDA) receptor AD antagonist (Memantine) thereby limiting its treatment possibilities. No new drugs have been approved for the treatment of AD since 2003.^{16,17} Decades of research in AD pathophysiology has led to target identification for new drug development. Nowadays, multi targeted directed ligands (MTDL) approach of AD therapy is widely used, where ChE inhibition is joined with additional biological properties.¹⁸ Drugs with neuroprotective and disease-modifying properties are of greater research interest. Multi-target-directed ligands (MTDL) strategy has been

used to develop a variety of hybrid compounds having capability to act simultaneously in diverse biological targets. The complex pathophysiology of AD may necessitate combination or multi drug targeted ligand therapy as disease modifying strategy.¹⁹ MTDLs approach involves molecular hybridization technique in which two or more pharmacophore of bioactive molecule are incorporated into single drug molecule. This approach reduces the side effects and lead to a better pharmacokinetic profile of the MTDL compared to two or more separate individual drug representing respective single pharmacophore.²⁰ This approach of discovery of drug candidate which is capable of targeting multiple factors involved in AD complex pathogenesis and having multiple properties like antioxidant, neuroprotective, metal chelation, anti-inflammatory, anti-A β aggregation and cholinesterase and secretase inhibitory activities, would greatly facilitate in improving therapeutic strategies.²¹

In this context, we have previously developed various multifunctional synthetic molecules against AD such as donepezil derivatives, indandione derivatives and diallyl disulphide derivatives.²²⁻²⁴ In the present work, we have rationally designed novel *N*-(6-methanesulfonyl-benzothiazol-2-yl)-3-(4-substituted-piperazin-1-yl)-propionamides as potential multifunctional agents for AD, which consists of benzothiazole moiety as well as piperazine moiety.

Benzothiazole are compounds with fused benzene and thiazole moiety containing nitrogen and sulphur, which has fascinated interest in central nervous system (CNS)-related drug discovery. Various studies have reported that benzothiazole derivatives possess a broad spectrum of biological activities

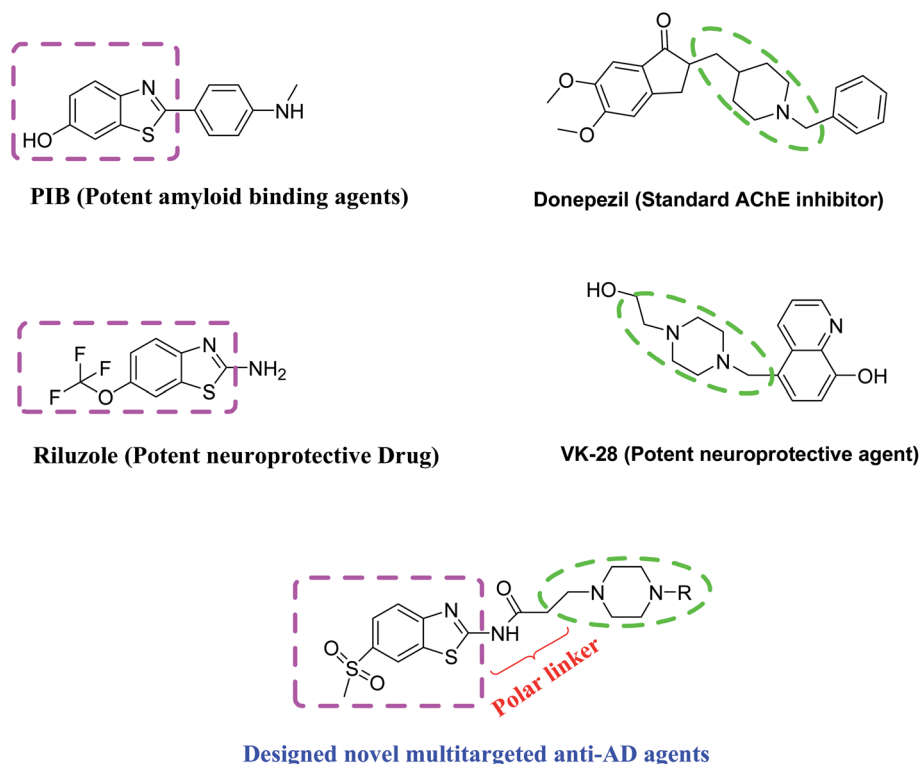


Fig. 1 Designing strategy of multifunctional benzothiazole–piperazine hybrids.



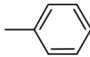
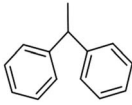

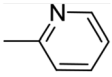
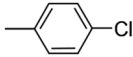
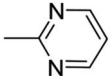
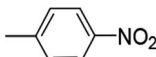
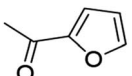
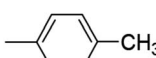
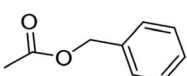
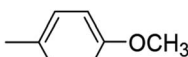
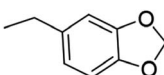
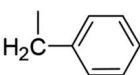
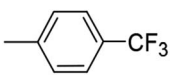
including AChE inhibitory action, A β -binding ability and neuroprotective property.^{25,26} For example, benzothiazole containing A β binding agents thioflavin-T and PIB are widely used in detecting amyloid fibrils *in vivo* as well *in vitro*.²⁷ Additionally, a well-known neuroprotective drug riluzole containing benzothiazole core has shown very potent neuroprotective effect in various *in vitro* as well as *in vivo* models and is widely used clinically for therapy of amyotrophic lateral sclerosis.²⁸ Moreover, benzothiazole derivative sabeluzole (NMDA antagonist), has also been reported to impede the clinical progression of AD.²⁹ Conversely, piperazine is a flexible ring system consisting of a six-member ring with two nitrogen atoms at 1, 4 positions. Piperazines are reported for various therapeutic uses and specially, this ring system has been widely used for CNS drug discovery.^{30–32} Studies have supported that piperazine derivatives show a very high binding affinity to amyloid, capability to cross blood brain barrier and in addition they also provide rapid elimination of non-specific signals from the brain.³³ Moreover, piperazines containing neuroprotective agents VK-28 as well as SP-04 are well studied as effective neuroprotective agents in various neurodegenerative models.³⁴

A lot of efforts have been made by several research groups to modify donepezil pharmacophore (standard AChE inhibitor) by various approaches such as bioisosteric replacement of pharmacophoric elements, hybridization of two pharmacophore, and linker optimization. Indeed, some of the modified leads have shown potential multifunctional activities for the treatment of AD.³⁵ It is well studied that basic piperidine moiety of standard AChE inhibitor donepezil actively participates in interaction with the AChE active site and this basic moiety is considered as an essential pharmacophoric element to produce inhibitory action.³⁶

Therefore, by considering these evidences benzothiazole-piperazine hybrid molecules have been designed to develop effective multifunctional agents against AD. In due course, benzothiazole and piperazine pharmacophore have been hybridized by using a flexible propanamide linker. We have made bioisosteric replacement of the piperidine ring of donepezil with piperazine ring and it was thought that this bioisosteric replacement may provide better pharmacological action against AD. Additionally, it is also assumed that the flexible propanamide linker will provide enough flexibility to hybrid pharmacophore for adequate adjustment at CAS as well as the PAS binding site of AChE active site. Thus, this drug designing strategy may confer a series of benzothiazole-piperazine hybrid molecules as potential multifunctional agents that might display polypharmacological action all in concert, such as AChE inhibition, A β disaggregation, and neuroprotection (Fig. 1). Synthesized compounds have been evaluated for their acetylcholinesterase (AChE) and butyrylcholinesterase (BuChE) inhibitory action, A β disaggregation activity, metal chelation potency and neuroprotective capability. Additionally, molecular docking and molecular dynamic (MD) simulation have also been carried out to explore molecular level interaction of these molecules with AChE and A β peptide. Moreover, *in vivo* efficacy of the most active compound was illustrated in the scopolamine induced mouse model of dementia.

2. Results and discussion

2.1. Synthesis

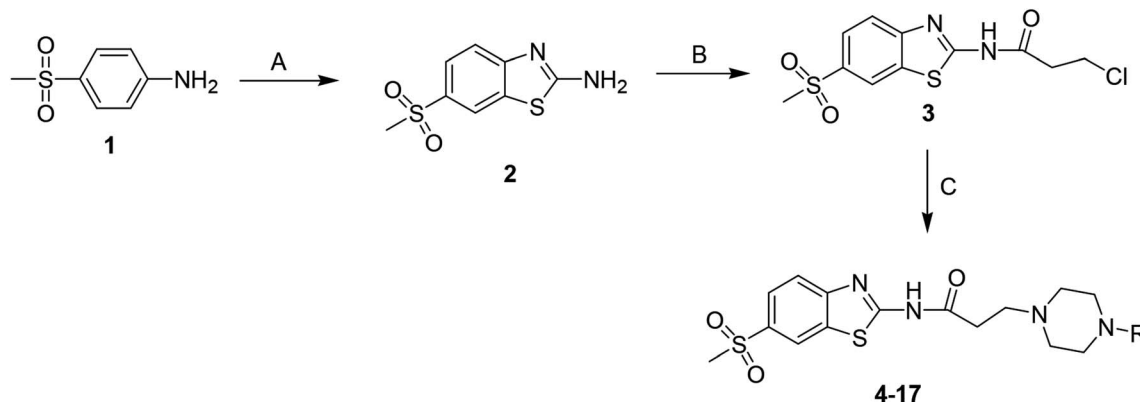
Compound number	R-group	Compound number	R-group
4 (85%)		11 (88%)	
5 (88%)		12 (74%)	
6 (75%)		13 (81%)	
7 (82%)		14 (69%)	
8 (84%)		15 (86%)	
9 (79%)		16 (75%)	
10 (76%)		17 (71%)	

Synthesis of designed benzothiazole-piperazine hybrids 4–17 have been carried out according to the conditions described in Scheme 1. Briefly, commercially available 4-methylsulfonyl aniline was stirred with potassium thiocyanate (KSCN) and Br₂ was added slowly to achieve benzothiazole-2-amine 1. Further, benzothiazole amine was reacted with 3-chloropropionyl chloride in 1,4-dioxane to give key intermediate 2 in high yield. Finally, substituted piperazine was coupled with key intermediate 2 by using a catalytic amount of NaHCO₃ and NaI to yield target compounds *N*-(6-methanesulfonyl-benzothiazol-2-yl)-3-(4-substituted-piperazin-1-yl)-propionamide 4–17. Synthesized molecules were completely characterized by ¹HNMR, ¹³C NMR and mass spectroscopy. Purity of target compounds were examined by reverse phase HPLC.

2.2. *In vitro* studies

2.2.1. Cholinesterase inhibitory activity and SAR discussion. The inhibitory potencies of synthesized hybrid molecules 4–17 were assessed against AChE and BuChE by following the well standard Ellman's method,³⁷ with donepezil as the reference drug. The inhibitory profile of these hybrid molecules for AChE and BuChE is presented in Table 1. As shown in Table 1, all target compounds exhibited moderate to good inhibition toward ChEs. On the basis of obtained inhibitory profile, following structure activity relationship has been observed. Compound 4, containing unsubstituted phenyl showed moderate inhibition towards AChE (IC₅₀ = 24.14 μ M). Hybrid molecules 5 (IC₅₀ = 18.31 μ M), 6 (IC₅₀ = 13.05 μ M) and 7 (IC₅₀ =





Scheme 1 Reagents and conditions: (A) KSCN, Br₂, glacial acetic acid, 0–5 °C, 6 h; (B) 3-Chloropropionyl chloride, TEA, 1,4-dioxane, reflux, 8 h; (C) Substituted piperazines, NaHCO₃, NaI, dried acetonitrile, reflux, 8–12 h.

Table 1 Inhibition of AChE, BuChE, and Aβ₁₋₄₂ aggregation by the synthesized compounds

Compounds	IC ₅₀ ± SD (μM) AChE ^a	IC ₅₀ ± SD (μM) BuChE ^b	Self Aβ ₁₋₄₂ aggregation inhibition ^c (%)
4	24.14 ± 0.721	>100	54.29502 ± 0.265
5	18.31 ± 0.777	>100	55.53029 ± 0.134
6	13.05 ± 0.813	>100	51.74112 ± 0.289
7	11.25 ± 1.803	>100	54.34428 ± 0.427
8	20.18 ± 1.435	>100	54.43522 ± 0.159
9	14.45 ± 1.032	>100	52.31708 ± 0.114
10	7.834 ± 0.810	>100	53.40836 ± 0.322
11	4.548 ± 0.984	>100	52.22614 ± 0.513
12	2.319 ± 0.410	>100	53.30605 ± 0.541
13	10.87 ± 0.657	>100	53.6736 ± 0.228
14	14.59 ± 0.438	>100	54.48827 ± 0.885
15	19.48 ± 0.452	>100	52.44591 ± 1.203
16	5.244 ± 0.690	>100	45.3109 ± 0.241
17	26.43 ± 0.551	>100	53.40836 ± 0.805
Rivastigmine	4.45 ± 0.37	1.32 ± 0.09	n.a. ^d
Galantamine	3.12 ± 0.44	3.12 ± 0.44	n.a. ^d
Tacrine	0.13 ± 0.21	0.054 ± 0.85	n.a. ^d
Donepezil	0.049 ± 0.05	8.71 ± 1.36	n.a. ^d
Curcumin	n.a. ^d	n.a. ^d	50.23 ± 1.201

^a Half maximal inhibitory concentration of AChE from electric eel (means ± SD of three experiments). ^b Half maximal inhibitory concentration of BuChE from equine serum (means ± SD of three experiments). ^c Self-induced Aβ₁₋₄₂ aggregation inhibition (50 μM) by tested inhibitors at 50 μM by thioflavin-T based fluorescence method (means ± SD of three experiments). ^d na-no activity.

11.25 μM), bearing electron withdrawing group F, Cl, NO₂ respectively displayed better inhibitory actions as compared to compound **4** which contains unsubstituted phenyl at the terminal end. Thus, substitution with electron withdrawing groups bestowed better inhibitory action as compared to unsubstituted counterpart, although this trend was not observed for compound **17** (IC₅₀ = 26.43 μM) which has electron withdrawing group CF₃. It was detected that derivatives **8** and **9**, bearing electron donating group, methyl as well as methoxy respectively showed slightly higher IC₅₀ value as compared to unsubstituted phenyl as well as with compounds having electron withdrawing group. However, the introduction of the flexible benzyl group (compound **10**) in this pharmacophore produced effective inhibitory action against AChE (IC₅₀ = 7.83 μM). Noticeably, introduction of one more phenyl moiety on

benzylic carbon (compound **11**) promisingly enhanced inhibitory action and this bulkier group containing compound showed an IC₅₀ value of 4.54 μM for AChE. Introduction of one nitrogen as heteroatom to terminal benzene ring (compound **12**) provided most active AChE inhibitor of the series with an IC₅₀ value in the low micromolar range (2.31 μM). This compound appeared as a most potent AChE inhibitor in the entire series, although, two nitrogen containing pyrimidine derivative **13** failed to give promising inhibitory action. Thus, it may be hypothesized that 2-pyridine at the terminal end of this pharmacophore is well tolerated inside the active site of AChE. Molecular docking study also confirmed adequate binding of this molecule in the active site of AChE. At the terminal end furoyl (compound **14**) as well as benzyl ester (compound **15**) was also not favourable to exert effective inhibition against AChE. A



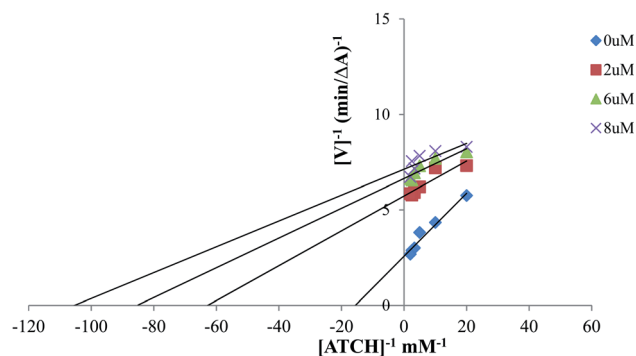


Fig. 2 Lineweaver–Burk reciprocal plot of AChE initial velocity with increasing substrate concentrations showing kinetic study of AChE inhibition mechanism with compound 12.

moderate IC_{50} value 10.87 and 14.59 μM were noticed for compound 14 and compound 15, respectively. Markedly, compound having piperonyl group (compound 16) showed low micromolar range inhibition ($IC_{50} = 5.24 \mu\text{M}$) against AChE. Thus, it may be hypothesized that flexible bulkier side group like piperonyl is also favourable in inhibiting AChE very effectively. Inhibition data for BuChE clearly indicate that none of the compounds showed inhibition to BuChE (IC_{50} value of $>100 \mu\text{M}$), indicating their high selectivity towards AChE. Such type of selective inhibition for AChE may be beneficial in reducing peripheral cholinergic side effects. The level of AChE is higher in the brain whereas the level of BuChE is higher in the blood. Thus, inhibition of BuChE will result into lower blood cholinesterase levels thus amplifying the risk of cholinergic distress by enhancing peripheral cholinergic side effects.^{38,39} BuChE has also been reported to be allied with metabolism of drugs and lipoproteins. Therefore, selective inhibition of AChE over BuChE is an important outlook for discovery of safe anti-alzheimer agents.^{40,41} For instance, AChE inhibitors used for the therapy of AD; donepezil, galantamine and rivastigmine, former two are selective AChE inhibitors and show better curative effects in contrast to the third which is non selective inhibitor. Also, tacrine, owing to its low selectivity for AChE showed extreme side effects,⁴² and ultimately has been withdrawn from market.

2.2.2. Kinetic characterization of AChE inhibition. The most potent compound 12 was further studied to get an insight into the mechanism of AChE inhibition by enzyme kinetics studies. The molecular docking studies revealed that the compound 12 was binding to both the CAS and PAS site, giving a mixed type of inhibition. However, the inverse of the reaction rates *versus* the inverse of substrate at different concentrations of the compound 12, Lineweaver–Burk reciprocal plots were formed (Fig. 2). Their Lineweaver–Burk reciprocal plots exhibited a decrease in V_{max} as well as K_{m} with increasing inhibitor (compound 12) concentration. The result revealed that compound 12 exhibited an uncompetitive type of inhibition.⁴³

2.2.3. Modulation of self-induced $A\beta_{1-42}$ aggregation. A major hallmark of AD is the formation of amyloid β ($A\beta_{1-42}$) peptides from amyloid precursor protein (APP) after cleavage by

γ -secretases and β -secretases. $A\beta_{1-42}$ folds into β -sheets, self-assembling into toxic fibrillar aggregates. These fibrillar aggregates (plaques) play a crucial role in initiating the pathophysiology of AD. Inhibition of the formation of fibrillar aggregates is one of the most prominent approaches to develop effective therapeutic agents for AD.⁴⁴ To study the effect of compounds 4–17 on the aggregation propensity of $A\beta_{1-42}$, a Thioflavin-T (ThT) assay was performed, curcumin was used as a reference (Table 1, Fig. 3a). Most of the compounds exhibited strong inhibitory activity against $A\beta_{1-42}$ aggregation and it was better than standard curcumin. These compounds have shown the percentage of inhibition ranging from 45.31% to 55.53% at the concentration of 50 μM . Hybrid molecule 12 which was very effective AChE inhibitor, also exhibited significant inhibition of $A\beta_{1-42}$ aggregation compared to the standard (Fig. 3b). Thus, these molecules are capable in inhibiting $A\beta_{1-42}$ aggregation effectively, being an effective inhibitor of AChE.

2.2.4. Confocal microscopy of compound 12 on $A\beta_{1-42}$ aggregation inhibition. The clearance of amyloid beta fibrils is an effective therapeutic strategy for AD treatment. Hence, the drug designed to combat AD should have the potential of removing $A\beta_{1-42}$ mature fibrils. The $A\beta_{1-42}$ aggregation activity of the most promising compound 12 was monitored by Confocal Laser Scanning Microscopy (CSLM) in order to complement the

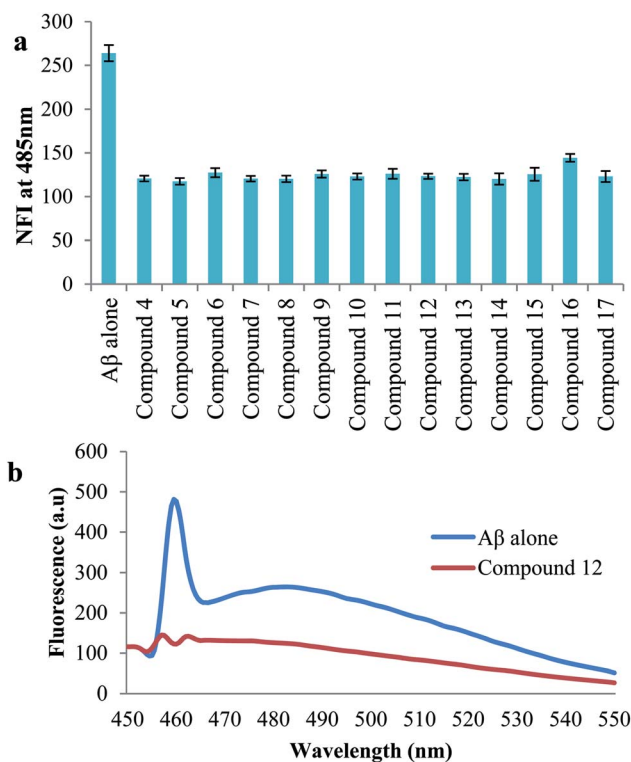


Fig. 3 (a) Inhibition of $A\beta_{42}$ aggregates studied by thioflavin (ThT) assay. $A\beta_{42}$ (50 μM) was incubated alone and independently with compounds and their influence on $A\beta$ aggregation was quantified by measuring ThT fluorescence intensity, represented as normalized fluorescence intensity (NFI) at 485 nm for a given time point (48 h); (b) ThT emission fluorescence spectra (range 450–550 nm) of $A\beta_{1-42}$ alone in blue and in the presence of compound 12 (50 μM) in red.



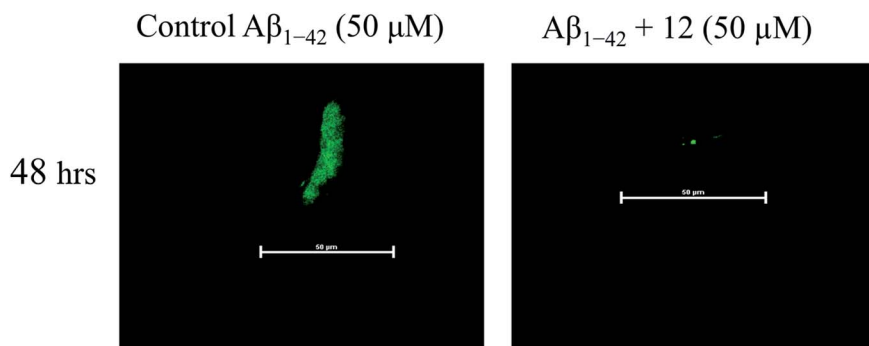


Fig. 4 Assessment of the effect of compound **12** on anti-aggregation property of amyloid beta peptide ($A\beta_{1-42}$). Confocal laser scanning microscopic analysis of the deposited amyloid beta aggregates as assessed in 48 h. The fluorescence intensity of confocal microscopic image represents a vision of $A\beta_{1-42}$ amyloid aggregates, with representative $A\beta_{1-42}$ peptide (control) co-incubated with the presence of compound **12**.

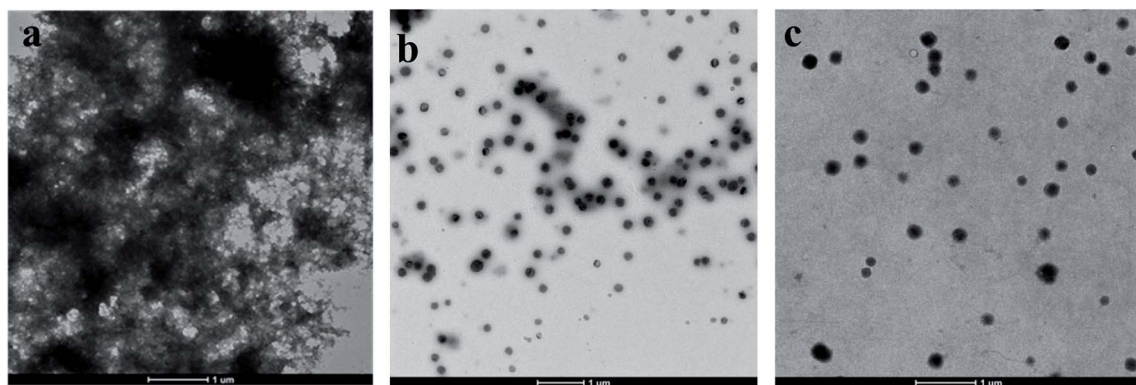


Fig. 5 TEM analysis of $A\beta_{1-42}$ aggregation in the presence of compound **12**: (a) $A\beta_{1-42}$ alone (50 μ M), incubated at 37 $^{\circ}$ C for 48 h. (b) $A\beta_{1-42}$ (50 μ M) and curcumin (50 μ M) were incubated at 37 $^{\circ}$ C for 48 h. (c) $A\beta_{1-42}$ (50 μ M) and **12** (50 μ M) were incubated at 37 $^{\circ}$ C for 48 h.

results of ThT binding assay, (Fig. 4). The higher fluorescence in confocal laser scanning microscopy images validated the noticeable fibrillar formation in $A\beta_{1-42}$ alone (control) group, and further, decrease in the fluorescence showed that $A\beta_{1-42}$ aggregation were inhibited when $A\beta_{1-42}$ was incubated with compound **12**. The results confirm that compound **12** proficiently prevents $A\beta_{1-42}$ fibril formation and has potential of $A\beta_{1-42}$ aggregation inhibition property.

2.2.5. TEM study of compound 12 on inhibition of $A\beta_{1-42}$ fibril formation. In line with the ThT binding assay and CSLM, most potent $A\beta_{1-42}$ aggregation inhibitor **12** was subjected to TEM analysis for studying its effect on $A\beta$ aggregation process. At 0 h time point, samples with $A\beta_{1-42}$ showed no aggregation (data not shown). While after incubating for 48 h at 37 $^{\circ}$ C, sample with $A\beta_{1-42}$ alone had typically aggregated into mature, bulkier and dense amyloid fibrils (Fig. 5a). In comparison, electron micrographs of $A\beta$ samples incubated with curcumin and compound **12** respectively under similar experimental conditions showed small dissociated aggregates and no characteristic fibrils of $A\beta_{1-42}$ (Fig. 5b and c). The results of TEM were in concordance with the results of ThT studies and CSLM studies, proving the effectiveness of compound **12** in slowing down the rate of $A\beta_{1-42}$ fibrils formation *in vitro*.

2.2.6. Disaggregation of self-induced $A\beta_{1-42}$ aggregation. The most active multipotent compound **12** displaying higher potential to inhibit self-mediated $A\beta_{1-42}$ aggregation was further evaluated for its ability to disaggregate self-induced $A\beta_{1-42}$ aggregation by ThT assay. At 37 $^{\circ}$ C for 24 h, fresh $A\beta$ peptides were incubated to assist the formation of fibrils. Compound **12** was then added to the sample mixture and incubated for

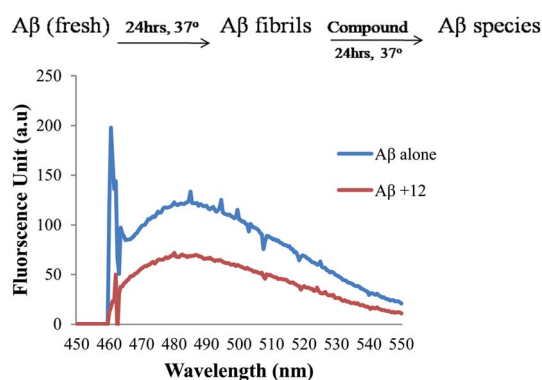


Fig. 6 ThT emission fluorescence spectra (range 450–550 nm) of $A\beta_{1-42}$ alone in blue and in the presence of compound **12** (50 μ M) in red for disaggregation studies.



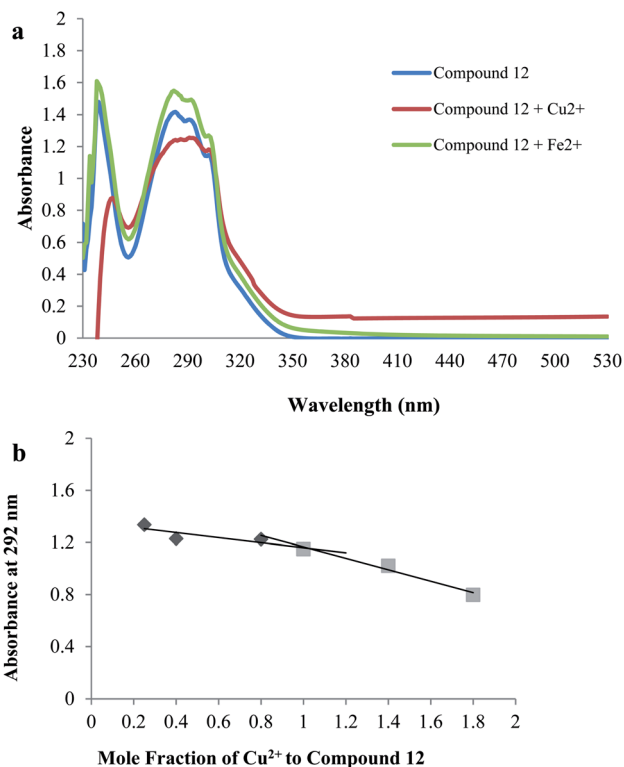


Fig. 7 Metal chelation study: (a) UV absorbance spectrum of compound **12** (60 μ M) alone in blue or in the presence of CuSO_4 (60 μ M) in red, FeSO_4 (60 μ M) in green in buffer (20 mM HEPES, 150 mM NaCl, pH 7.4); (b) determination of the stoichiometry of complex Cu^{2+} -**12** by Job's method.

another 24 h. Disaggregation studies were assessed by ThT assay, where fluorescence intensities indicate the degree of A β fibrillar aggregation. Compound **12** showed 48.64% disaggregation (Fig. 6), which implies that it can proficiently inhibit the already formed amyloid beta plaque.

2.2.7. Metal chelating properties of compound 12. The ability of our synthesized compound **12** to chelate bio-metals like Cu(II) and Fe(II) was performed by UV-vis spectroscopy.²³ On the addition of CuSO_4 into reaction mixture with compound **12**, it was observed that there was a visible bathochromic shift in the maximum absorption wavelength from 239 nm to 246 nm and 284 nm to 293 nm, and the absorbance also dropped noticeably, signifying the formation of a compound **12**-Cu(II) complex (Fig. 7a). The compound did not show any activity with ferrous ion. Job's method was employed to calculate the stoichiometry of the **12**-Cu(II) complex⁴⁵ by preparing a series of reaction mixture by varying the proportion of the metal ion and compound and keeping the total concentration constant. The absorbance of the complex of CuSO_4 and compound **12** at different concentrations were determined using UV spectroscopy. As shown in Fig. 7b, the absorbance change at 333 nm were plotted, the two straight lines intersected at a mole fraction of 1 implying a 1 : 1, **12**-Cu(II) complex.

2.2.8. Molecular docking studies. Additionally, to explore the interaction mode of hybrid molecule **12** with AChE (PDB code: 1EVE) and A β_{1-42} (PDB code: 1IYT), a molecular docking simulation study was performed using the Autodock 4.2 software.²² Compound **12** showed good interaction within the active site of AChE. As illustrated in Fig. 8, this compound was binding simultaneously to both the enzymatic catalytic active site (CAS) and the peripheral anionic site (PAS). It was visualized that benzothiazole core oriented towards CAS site and pyridine piperazine moiety engaged with PAS site. It was also noticed that propanamide linker have provided suitable length between CAS binding group as well as PAS binding group. Additionally, amide group of propanamide linker is also being involved in hydrogen bond interaction, which may provide stability of ligand within active site of AChE. His440, Phe288, Ser286 are involved in H-bond interaction with hybrid molecule **12** (Fig. 8). In mid-gorge sites, a hydrogen bond with the residue his440 and a cation- π interaction with ser200 and glu199 were

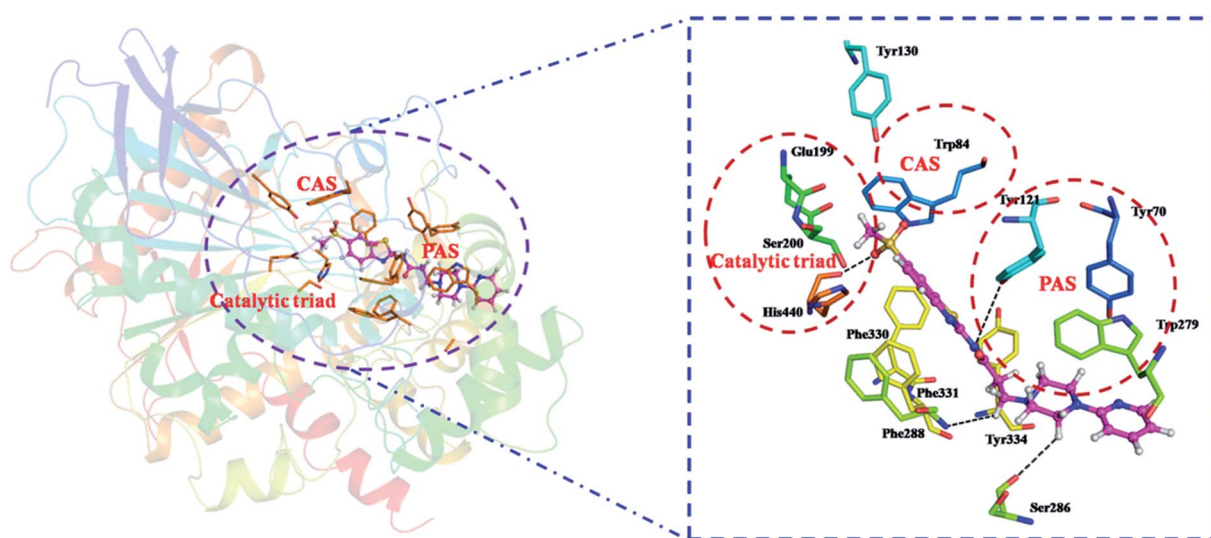


Fig. 8 Proposed binding mode of compound **12** in the active site of AChE (PDB: 1EVE). The black dashed lines represent hydrogen bonds.



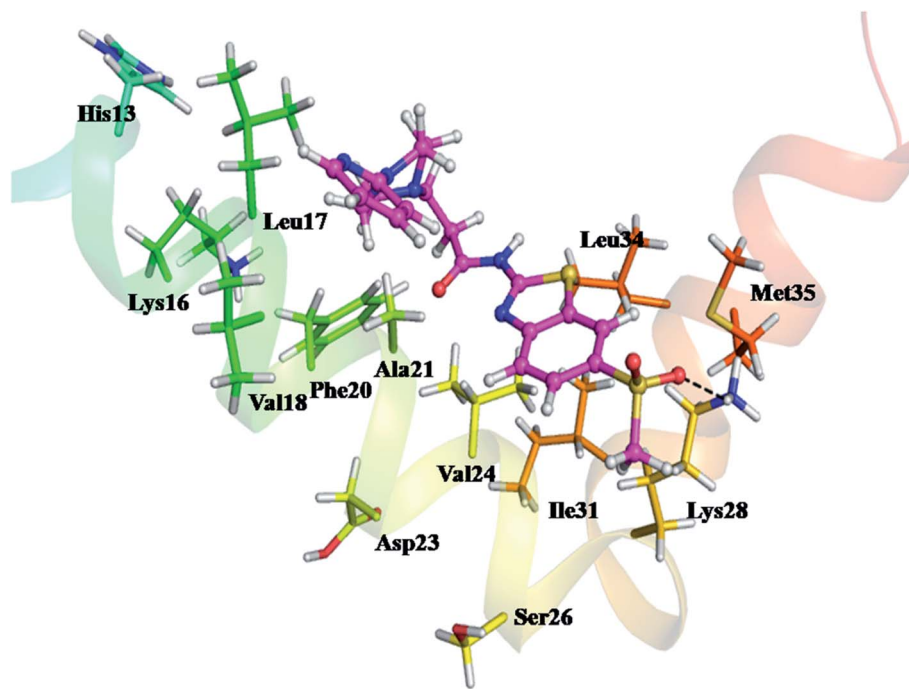


Fig. 9 Proposed binding mode of compound **12** in the active site of $A\beta_{1-42}$ (PDB: 1IYT). The blue dashed lines represent hydrogen bonds.

observed and could enhance the interaction with AChE. Trp279 and Tyr334 at PAS are involved in π - π stacking interaction with pyridine moiety of compound **12**. Additionally, compound **12** suitably interacts with CAS site and their benzothiazole moiety imparts hydrophobic interaction with CAS site residue Trp84.

Assessment of Fig. 9 to understand the binding mode of compound **12** with $A\beta_{1-42}$ shows that compound **12** interacts well with $A\beta_{1-42}$. Compound **12** is transversely fitted along the major helix, and Lys28 is involved in H-bond interaction with a methylsulfonyl group of compound **12**. In addition, propanamide and pyridine piperazine fragments display hydrophobic interactions with residues Lys16, Leu17, Val18, Phe20, Ala21, Asp23, Val24, ser26, Ile31, Leu34 and Met35 resulting in stabilized compound **12**- $A\beta_{1-42}$ complex very nicely. These results indicate that the hydrophobic interactions and the hydrogen bonding interaction play crucial roles in the effective inhibition of $A\beta_{1-42}$ aggregation.

2.2.9. Molecular dynamics (MD) simulation studies with AChE and $A\beta_{1-42}$. We have completed molecular dynamics (MD) simulation for 100 ns to examine the structural stability and molecular interaction of protein (AChE and $A\beta_{1-42}$)²² and complex with compound **12**. To examine the structural stability of AChE and AChE-**12** complex, we computed the time evolution plot of all C α -atom RMSD (Fig. 10a). It can be seen that the conformational dynamics of AChE remains stable around RMSD value 0.15 nm during the simulation of 100 ns in water at 300 K. The RMSD trajectory archives equilibrium \sim 20 ns and the stable equilibrium is observed up to \sim 65 ns. The small drift of 0.05 nm arises \sim 75 ns, however, the equilibrium is regained \sim 85 ns, suggesting the stable structural dynamics of protein in water. The RMSD plot of AChE-**12** complex shows initial

increase in RMSD of 0.05 nm during 0–10 ns, the consequences of small drifts of \sim 0.02–0.04 nm can be seen at 10–25 ns and the quite stable trajectory during 25–100 ns. The initial drifts in plot represented the structural perturbation arises due to protein–ligand interactions which is finally settled around 25 ns and we can observe the stable conformational dynamics of AChE-**12** complex till the simulation end at 100 ns.

Another effective parameter, radius of gyration (R_g) is applied to investigate the conformational stability and integrity of protein and protein–ligand complex⁴⁶ (Fig. 10b). The R_g plot of all C α -atoms shows that the structural composition of AChE is retained in water, having R_g value 2.30 ± 0.02 nm. However, the structural integrity of AChE-**12** complex remains stable around R_g value 2.27 ± 0.02 nm. This slight decrease in R_g value indicates the stable molecular interaction of protein–ligand complex.

To determine the structural stability of AChE and AChE-**12** complex we also monitored the solvent accessible surface area (SASA) as shown in Fig. 10c. We observed that the structure of both, AChE and AChE-**12** complex having almost similar average SASA value \sim 310 nm². This result suggested that the ligand is nicely fitted at the active site of AChE, thus, the conformational dynamics analyses RMSD, R_g and SASA results were consistent, indicating the stable interaction of AChE-**12** complex.

To investigate conformational fluctuations, and the effect of local dynamics on the structural complex of AChE-**12**, and residues involved in molecular interaction, we calculated the average fluctuation of each amino acids of AChE. The RMSF plot of all C α -atoms is shown in Fig. 10d. The RMSF results clearly indicate that the active site residues which were involved in



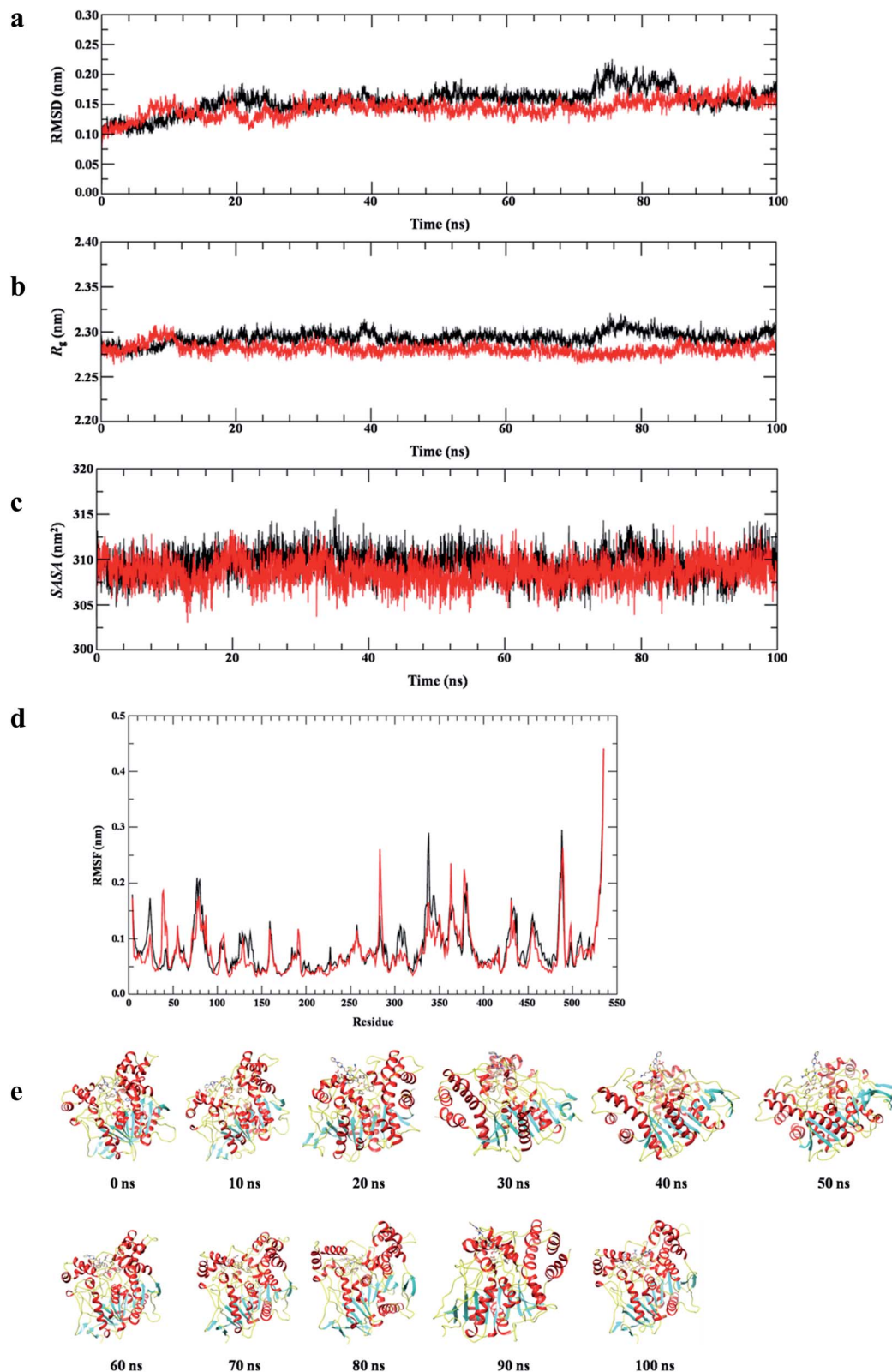


Fig. 10 Molecular dynamic simulation studies with AChE (a) The equilibrium average of C^α RMSD of AChE (black), AChE-12 docked complex (red) in water at 300 K; (b) time evolution plot of radius of gyration (R_g) plot of AChE (black), AChE-12 complex (red) in water at 300 K; (c) time evolution plot of solvent accessible surface area (SASA) plot of AChE (black), AChE-12 complex (red) in water at 300 K; (d) root mean square fluctuation (RMSF) plot of AChE (black), AChE-12 complex (red) in water at 300 K; (e) structural snapshot of AChE-12 complex at the time interval of 10 ns, during the simulation in water at 300 K.



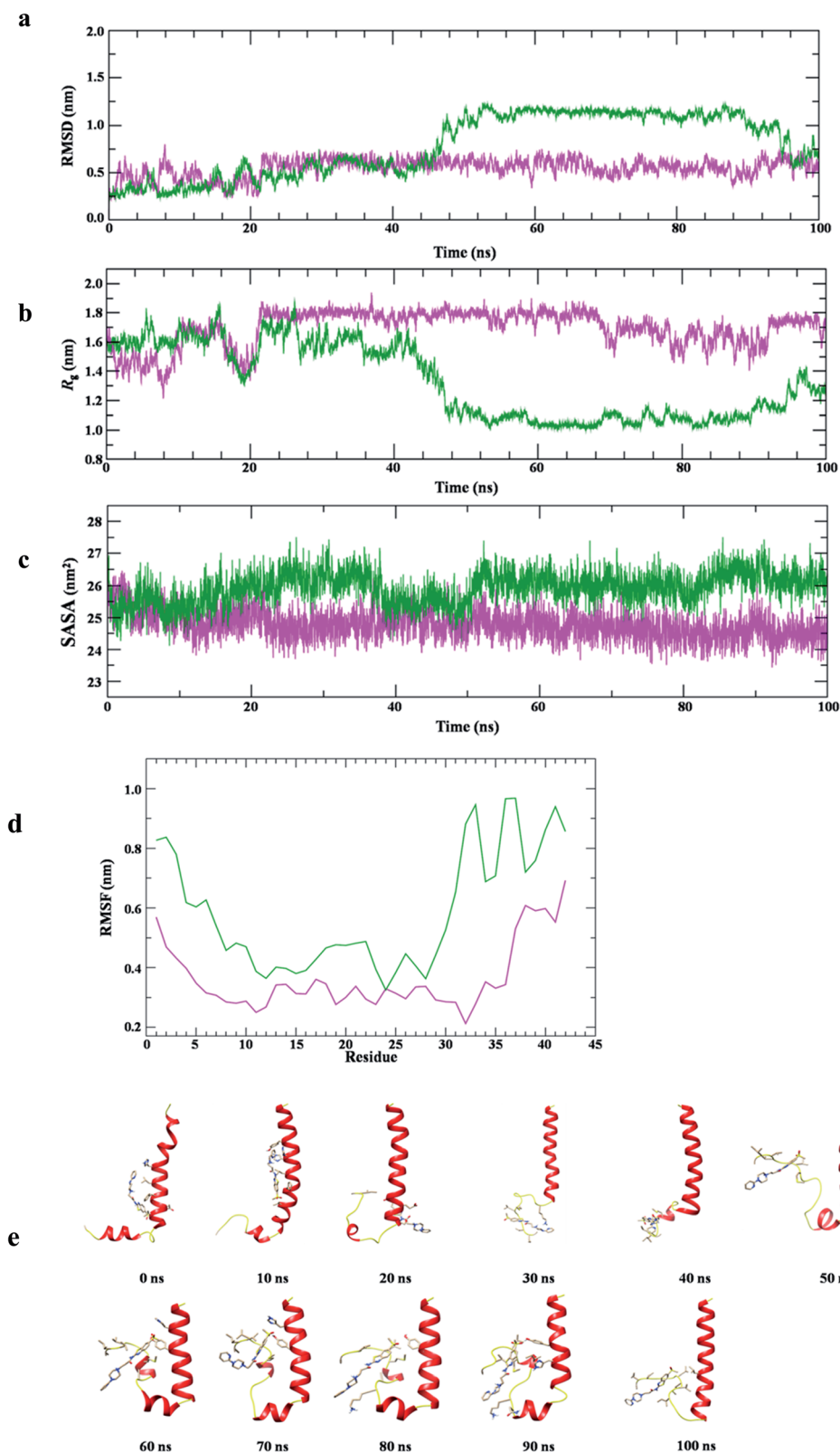


Fig. 11 Molecular dynamic simulation with $A\beta_{1-42}$: (a) the equilibrium average of C^α RMSD of $A\beta_{1-42}$ (magenta), $A\beta_{1-42}$ -12 docked complex (green) in water at 300 K; (b) time evolution plot of radius of gyration (R_g) plot of $A\beta_{1-42}$ (magenta), $A\beta_{1-42}$ -12 docked complex (green) in water at 300 K; (c) time evolution plot of solvent accessible surface area (SASA) plot of $A\beta_{1-42}$ (magenta), $A\beta_{1-42}$ -12 docked complex (green) in water at 300 K; (d) root mean square fluctuation (RMSF) plot of $A\beta_{1-42}$ (magenta), $A\beta_{1-42}$ -12 docked complex (green) in water at 300 K; (e) structural snapshot of $A\beta_{1-42}$ -12 complex at the time interval of 10 ns, during the simulation in water at 300 K.



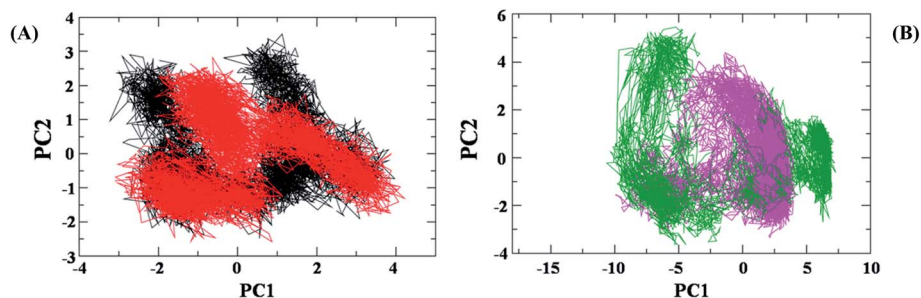


Fig. 12 Principal component (PC) analysis of protein and protein–ligand complex: (A) the collective motion of AChE (black), AChE–12 complex (red) using projections of MD trajectories on two eigenvectors corresponding to the first two PCs. (B) $A\beta_{1-42}$ (green) and $A\beta_{1-42}$ –12 docked complex (magenta).

interaction with compound **12** having lower average fluctuation. Furthermore, the almost complete overlapping RMSF plots of AChE and AChE–12 complex signifies no conformational changes in native structure of protein upon the binding of ligand. Thus, to confirm the results we also measured the evolution plot of secondary structure (ESI Fig. S1 and S2[†]) and the structural snapshots of AChE–12 (Fig. 10e) at time interval of 10 ns. Both analyses show consistent results with RMSF which again confirm the favourable interaction of **12** at active site of AChE.

The conformational stability of $A\beta_{1-42}$ –12 complex was measured using structural order parameters, RMSD, R_g and SASA. Fig. 11a shows that RMSD plot of $A\beta_{1-42}$ remains stable around 0.5 nm in water at 300 K. The consecutive drifts in trajectory, during the initial 0–20 ns represents the flexible nature of $A\beta_{1-42}$, however, it attains equilibrium at ~ 20 ns and the stable structure can be seen for 20–100 ns of simulation. However, the plot shows lower RMSD value upon binding with **12**, during initial 0–25 ns of simulation. The trajectory of $A\beta_{1-42}$ –12 complex finds stable at 25–40 ns, followed by continuous increase in RMSD ~ 40 –55 ns. With the drift of ~ 0.5 nm which suggested the conformational flipping, it attains stable equilibrium at ~ 55 –95 ns and during the last 5 ns, it dropped down to the conformational state observed for ligand unbound $A\beta_{1-42}$.

The comparative structural stability and integrity of $A\beta_{1-42}$ and $A\beta_{1-42}$ –12 complex examined by R_g plot (Fig. 11b) shows initially flexible R_g trajectory for $A\beta_{1-42}$ which attains equilibrium ~ 20 ns and structural dynamics remains stable with average R_g value 1.8 ± 0.02 nm for the period of 20–100 ns. Differently, the R_g plot of $A\beta_{1-42}$ –12 complex shows initial fluctuation around R_g value 1.8 nm which is dropped down to 1.3 nm at ~ 20 ns, thereafter, with the drift of 0.3 the trajectory remains fluctuating around R_g value 1.6 which can be observed during 24–40 ns. We find subsequent decrease in R_g value ~ 48 ns and the stable conformation of protein–ligand complex with R_g value 1.1 nm is observed during the period of 50–100 ns of simulation. Thus, the R_g analysis also anticipated the two major conformational states of $A\beta_{1-42}$ –12 complex. However, the SASA plot (Fig. 11c) of $A\beta_{1-42}$ remains stable ~ 26 nm², whereas, we find slightly lower SASA value (~ 25 nm²) as compared protein alone in water. This observation suggested the stable association of **12** with $A\beta_{1-42}$. We also examine RMSF plot (Fig. 11d) to

understand the contribution of active site residues on conformational stability of $A\beta_{1-42}$ –12 complex. RMSF plot shows that the residues belonging to $A\beta_{1-42}$ having average fluctuation ≤ 0.4 nm, whereas, the average fluctuation of $A\beta_{1-42}$ is slightly increases upon binding with **12**. The secondary structure analysis shows that the helical structure of $A\beta_{1-42}$ remains consistent with crystal structure, however, we observed the propensity to form turn like structure for the residues belonging to N- and C-terminal of $A\beta$ (ESI Fig. S3 and S4[†]). The binding of **12** disrupted the salt bridge between the Asp23–Lys28 which prevent the self-aggregation of $A\beta_{1-42}$, thus, we observed turn like structure at C-terminal of $A\beta_{1-42}$ –12 complex, however, the helical structure of $A\beta$ at N-terminal remains consistent with crystal structure. The structural snapshot of $A\beta_{1-42}$ –12 complex at the time interval of 10 ns (Fig. 11e) provide the clear evidence that binding interaction of **12** is largely localized at the C-terminal and the bulky side chain of **12** create structural hindrance for salt bridge associated, thus prevent the protein aggregation the pathological state of Alzheimer disease.⁴⁷

To further explore the dynamic properties of the investigated structures in our simulations, the essential dynamics (ED) analysis on the $C\alpha$ atoms was performed.⁴⁸ ED actually reflects the overall conformational space of protein and protein–**12** complex during simulations (Fig. 12A). The projection of

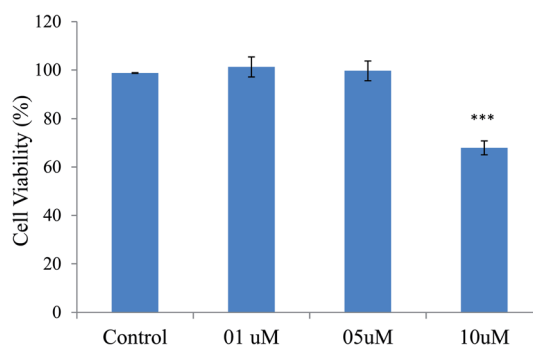


Fig. 13 Effects of various concentrations of compound **12** on cell viability in SHSY5Y cells after treatment for 24 h. Cell viability was measured by MTT assay. Data were shown as mean \pm SD of three independent experiments and each included triplicate sets. *** $p < 0.001$ vs. control, statistical analysis was performed.



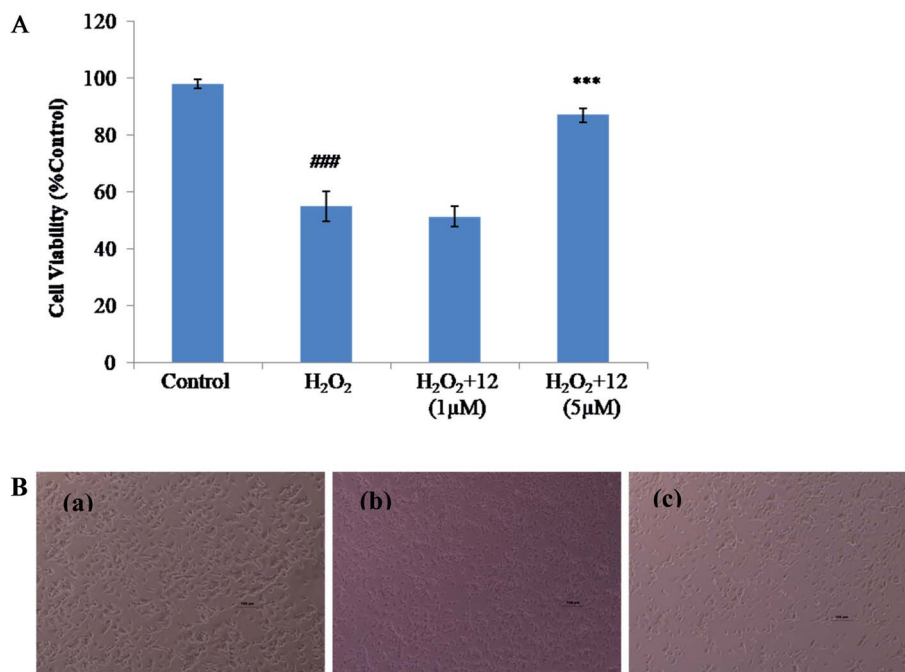


Fig. 14 A: Protective effects of compound **12** on H₂O₂-induced cell death in SHSY5Y cells. Cells were incubated with different concentration of **12** for 3 h and then treated with 200 μM H₂O₂ for 24 h. Cell viability was measured by MTT assay. Data were shown as mean ± SD of three independent experiments and each included triplicate sets. ###*p* < 0.001 compared to control, ****p* < 0.001 compared to H₂O₂ treated cells; B: phase-contrast micrographs showing morphological changes in H₂O₂-induced neurotoxicity and neuroprotection of compound **12** in SH-SY5Y cells. (a) Cells without treatment showed healthy shapes. (b) H₂O₂ alone (200 μM) induced neurotoxicity. (c) Co-treatment of compound **12** (5 μM) for 24 h with H₂O₂ (200 μM) and showed neuroprotection.

trajectories onto the first two principal components (PC1, PC2) shows the motion of investigated system: AChE and AChE-12 complex in phase space and is illustrated in Fig. 12A.

In the ED analysis shows, both AChE and AChE-12 complex show similar phase space behaviour, however, the ligand **12** decreases the flexibility in the AChE protein which is suggesting the normal function of the protein upon complex formation with **12**.

Differently, the ED analysis of Aβ₁₋₄₂ and Aβ₁₋₄₂-12 complex shows that the protein-12 complex has not explored the same conformational space as the native protein, Aβ₁₋₄₂ (Fig. 12B). Instead, it is restricted to small excursions slightly away from its initial conformation. In this Fig. 12B, we can see irregular stretches or clusters of line in the ED plot of Aβ. Two features are very apparent from these plots. Firstly, the clusters are well defined in Aβ₁₋₄₂-12 complex structure than the protein Aβ₁₋₄₂ alone. Secondly, the Aβ-12 complex covers a smaller region on the plot particularly along PC1 plane compared to that covered by native Aβ₁₋₄₂. It is also clear from all the plots that the flexibility of Aβ₁₋₄₂ decreases upon binding to **12**, suggesting that **12** can efficiently prevent the self-aggregation of Aβ₁₋₄₂, the pathological state of Alzheimer disease.^{49,50} Our observation thus corroborates with the idea of higher flexibility of Aβ₁₋₄₂ at 300 K.

2.2.10. In vitro cytotoxicity assay. Compound **12** possessing AChE inhibition, metal ions chelation and Aβ₁₋₄₂ aggregation inhibition was further evaluated for cytotoxicity studies in the human neuronal cell line SHSY5Y. SH-SY5Y cells were exposed to compound **12** at different concentrations (1, 5 and 10 μM) for

24 h, and cell viability assay was performed using the 3-(4,5-dimethyl dimethylthiazol-2-yl)-2,5-diphenyltetrazolium (MTT). As given in Fig. 13, no cytotoxicity was displayed by the compound **12** at concentrations of 1 and 5 μM after incubation for 24 h. When the concentration was increased up to 10 μM, compound **12** displayed more than 67% cell viability. Hence, these results suggest that compound **12** exhibits very low toxicity to SHSY5Y cells in the range of tested concentrations.

2.2.11. Neuroprotection against H₂O₂-induced death in SH-SY5Y cells. The ability of compound **12** to provide neuroprotection against H₂O₂-induced damage in SH-SY5Y cells were assessed using a cell viability assay at two concentrations: 1 and 5 μM. It was observed in the Fig. 14A and B that exposing SH-SY5Y cells with H₂O₂ for 24 h resulted in a considerable decrease in cell viability (54.90%, ###*p* < 0.001). However, when the cells were treated with the test compound **12** along with H₂O₂, it was found that the compound **12** imparted significant neuroprotection at concentration 5 μM. Hybrid molecule **12** induced marked cellular recovery at this concentration (86.96%, ****p* < 0.01), as compared to the H₂O₂-treated cells. Thus, it proves our hypothesis that the tested hybrid molecule display neuroprotection against H₂O₂ induced neurotoxicity through its ability to block H₂O₂ mediated oxidative stress and damage.

2.3. In vivo studies

The clinical manifestation of dementia is the impairment of learning as well as memory and is considered as a main

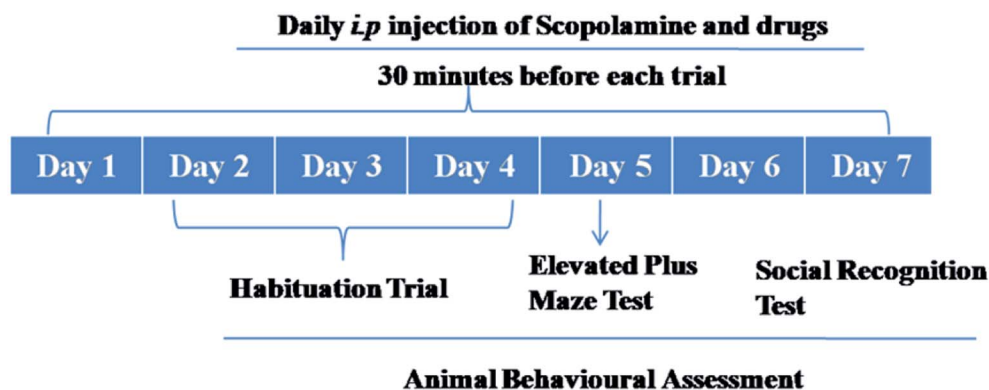


symptom of AD. Scopolamine is a known muscarinic receptor antagonist that interferes with transmission of acetylcholine in the central nervous system⁵¹ inducing dysregulation in cholinergic signaling pathway causing severe damage in learning, and short term maintenance of spatial memory tasks. Therefore, anti-dementia and nootropic effect compound 12 was evaluated against scopolamine-induced mice model of dementia.

2.3.1. Effect of compound 12 on transfer latencies by EPM test.

Compound 12 at both the doses showed significant reductions of transfer latencies (Table 2), which indicates its anti-dementia and nootropic potential against scopolamine induced memory deficit.

2.3.2. Effect of compound 12 in social recognition test. To study the ability of compound 12 in enhancing cognition in scopolamine induced mice, well distinguished social recognition test was performed.⁵³ The results indicated a significant decrease in the T_2/T_1 ratio (second interaction trial/first



For the study of learning and memory in rodents which relies on the intrinsic tendency of mice to stay in closed spaces, EPM model is used widely.⁵² Therefore, compound 12 was evaluated for anti-amnesic activities in this model. During the training trial, our result showed no significant difference in the transfer latencies among the treatment groups in EPM *i.e.* all the mice of the different groups came into the closed arm of the maze within stipulated time period. Nonetheless, in the scopolamine treated group (3 mg kg^{-1}), the transfer latency time increased significantly when compared to the control group, which indicated the memory impairment during the retention trial (Table 2). In comparison, there were significant reduction in the transfer latency in the donepezil (5 mg kg^{-1}) treated group that showcased its potential in reversing memory impairment induced by scopolamine.

Similarly, animals treated with compound 12 at 10 mg kg^{-1} and 20 mg kg^{-1} significantly reversed the effects of scopolamine.

interaction trial ratio) after treatment with compound 12 as compared to the scopolamine treated group. This suggests that compound 12 significantly enhanced the short-term memory. Our results indicated that compound 12 at 20 mg kg^{-1} have shown a T_2/T_1 ratio 0.377 ± 0.00072 as compared to scopolamine (3 mg kg^{-1}) and standard drug donepezil (5 mg kg^{-1}) treated group which displayed a T_2/T_1 ratio 1.103 ± 0.037 and 0.555 ± 0.133 respectively (Fig. 15). Thus, these results evidently support cognition enhancing ability of benzothiazole-piperazine hybrid molecule 12.

Table 2 Treatment effect of test compound 12 on the transfer latency (T_L) by EPM (elevated plus maze) test in scopolamine induced mice model of dementia

Groups	Transfer latency (T_L) in seconds ^a
Group 1 vehicle	9.82 ± 1.42
Group 2 scopolamine	22.00 ± 0.81
Group 3 scopolamine + donepezil	15.08 ± 1
Group 4 scopolamine + 12 (10 mg kg^{-1})	12.81 ± 2.08
Group 5 scopolamine + 12 (20 mg kg^{-1})	12.62 ± 2.60

^a Data is expressed as SEM of $n = 6$.

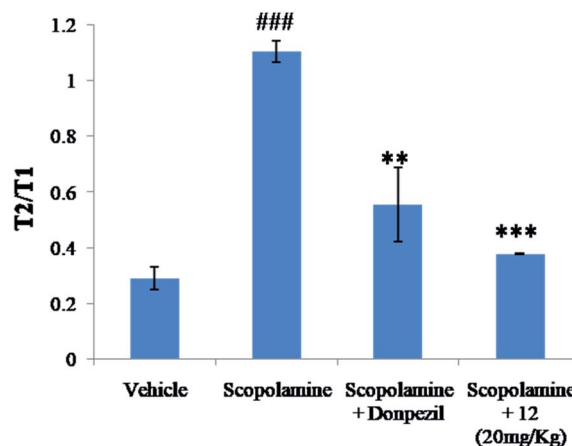


Fig. 15 Treatment effect of test compound 12 at 20 mg kg^{-1} on the T_2/T_1 (second interaction trial/first interaction trial ratio) in social recognition test in scopolamine induced model. Data is expressed as mean SEM of 6 animals. ### $p < 0.001$ compared to vehicle, *** $p < 0.001$ and ** $p < 0.01$ compared to scopolamine treated groups.



3. Conclusion

In conclusion, a series of multifunctional benzothiazole-piperazine hybrids (4–17) were developed to target multifaceted nature of Alzheimer's disease. The synthesized derivatives potentially and selectively inhibited AChE over BuChE with IC_{50} in micromolar range. Furthermore, the derivatives inhibited $A\beta_{1-42}$ aggregation efficiently. The results obtained from numerous *in vitro* and *in vivo* experiments established the multimodal mechanism of action of most active compound 12. In molecular docking studies, compound 12 adequately interacts with AChE and $A\beta$ peptide. Further, we performed MD simulation for compound 12 which reveals its proficient binding with AChE and $A\beta$ and steady interaction with the vital active site residual during 100 ns simulation. Compound 12 was non-cytotoxic to neuronal cells SHSY-5Y. This compound could efficiently reduce death induced by H_2O_2 treatment in the SHSY-5Y cells. It potentially attenuated scopolamine-induced cognitive impairments in mice model in the EPM and social recognition behavioral assays. Therefore, these properties together proved the multifunctional nature of 12, and its ability to alleviate multifaceted nature of AD. Furthermore, there is an enormous possibility for further development of this best lead molecule. Efforts in enhancing the efficiency of compound 12 through various chemical modifications have already been instigated by this research group.

4. Experimental methods

4.1. General

All the reagents and dried organic solvents were obtained from Sigma Aldrich (St. Louis, MO, USA.), TCI Chemicals (Tokyo, Japan), and Merck (Darmstadt, Germany). 1H and ^{13}C NMR spectra were acquired with a Jeol NMR spectrophotometer USA at 400 and 100 MHz, respectively. Chemical shifts are shown in parts per million (ppm) proportional to tetramethylsilane (TMS). The coupling constants (J) are presented in hertz (Hz), and the splitting patterns are designated by using abbreviations: s (singlet), d (doublet), t (triplet), m (multiplet), brs (broad singlet), and dd (double doublet). LC/MS data were recorded with an Agilent 6310 Ion trap LC/MS system and elemental analysis (C, H and N) was carried out on Elementar analysensysteme. Melting points were taken in open capillaries by using KSP11 melting point apparatus (KRUSS, Germany). Purity of all target compounds were analysed by using Shimadzu reverse phase HPLC system (Kyoto, Japan) coupled with a photodiode array detector (PDA) and C-18 column. Acetonitrile and methanol (80 : 20) were used as a mobile phase, keeping flow rate 1 ml min^{-1} . All target compounds displayed >97% purity.

4.2. Synthesis of 6-methanesulfonyl-benzothiazol-2-yl amine (1)

4-Methylsulfonyl aniline (10 millimole) and potassium thiocyanate (40 millimole) were stirred in glacial acetic acid at room temperature (RT) for 1 h. After that, bromine (10 millimole in

10 ml glacial acetic acid) was added dropwise by keeping temperature $0-5\text{ }^\circ\text{C}$. After addition of bromine, reaction was continued for 6 h at RT. Salt appeared in reaction mixture was filtered and dissolved in water. Salt solution was treated with ammonium hydroxide to give benzothiazole-2-amine in good yield.

4.2.1. 6-Methanesulfonyl-benzothiazol-2-yl amine (1). Yellow solid; yield 75% (1.71 g); mp $216-218\text{ }^\circ\text{C}$. 1H -NMR (400 MHz, DMSO- D_6) δ 8.21 (s, 1H), 7.95 (s, 2H), 7.67 (d, $J = 10.4\text{ Hz}$, 1H), 7.43 (d, $J = 8.5\text{ Hz}$, 1H), 3.13 (s, 3H); LC-MS: m/z ; 229 ($M + 1$).

4.3. Synthesis of 3-chloro-*N*-(6-methanesulfonyl-benzothiazol-2-yl)-propionamide (3)

An equimolar amount of benzothiazole amine 1 (10 millimole), 3-chloropropionyl chloride (10 millimole) and TEA (catalytic amount) were refluxed in 1,4-dioxane. Reaction mixture was poured in chilled water and obtained precipitate was filtered to give key intermediate 3-chloro-*N*-(6-methanesulfonyl-benzothiazol-2-yl)-propionamide (2).

4.3.1. 3-Chloro-*N*-(6-methanesulfonyl-benzothiazol-2-yl)-propionamide (2). White solid; yield 72% (2.28 g); mp $198-199\text{ }^\circ\text{C}$; 1H -NMR (400 MHz, DMSO- D_6) δ 12.77 (s, 1H), 8.62 (s, 1H), 7.91 (s, 2H), 3.89 (t, $J = 6.2\text{ Hz}$, 2H), 3.03 (t, $J = 6.3\text{ Hz}$, 2H); LC-MS: m/z ; 319 ($M + 1$).

4.4. Synthesis of *N*-(6-methanesulfonyl-benzothiazol-2-yl)-3-(4-substituted-piperazin-1-yl)-propionamide (4–17)

An equimolar ratio of key intermediate 3 and substituted piperazines were refluxed in acetonitrile with catalytic amount of $NaHCO_3$ and NaI for 8–14 h. Reaction mixture was diluted with water and crude product was extracted with ethyl acetate, dried with anhydrous sodium sulphate. Evaporation of ethyl acetate under reduced pressure was provided crude products. Crude products were purified with column chromatography using chloroform and methanol (90 : 5) to give pure target compounds 4–17 in very good yield.

4.4.1. *N*-(6-Methanesulfonyl-benzothiazol-2-yl)-3-(4-phenyl-piperazin-1-yl)-propionamide (4). White solid; yield 85% (205.6 mg); mp $201-202\text{ }^\circ\text{C}$. 1H -NMR (400 MHz, DMSO- D_6) δ 8.59 (s, 1H), 7.89 (s, 2H), 7.16 (t, $J = 7.6\text{ Hz}$, 2H), 6.88 (d, $J = 8.2\text{ Hz}$, 2H), 6.72 (t, $J = 7.3\text{ Hz}$, 1H), 3.20 (s, 3H), 3.08 (s, 4H), 2.71 (s, 4H), 2.55 (t, $J = 4.1\text{ Hz}$, 4H); ^{13}C -NMR (100 MHz, DMSO- D_6) δ 172.5, 162.1, 152.7, 151.1, 136.1, 132.0, 129.4, 125.7, 122.8, 121.3, 119.3, 115.2, 53.6, 52.3, 44.0, 33.3; LC-MS: m/z ; 445 ($M + 1$); anal. calcd for: $C_{21}H_{24}N_4O_3S_2$; C, 56.73; H, 5.44; N, 12.60; found: C, 56.99; H, 5.68; N, 12.42.

4.4.2. 3-[4-(4-Fluoro-phenyl)-piperazin-1-yl]-*N*-(6-methanesulfonyl-benzothiazol-2-yl)-propionamide (5). White solid; yield 88% (196.8 mg); mp $200-202\text{ }^\circ\text{C}$. 1H -NMR (400 MHz, DMSO- D_6) δ 8.59 (s, 1H), 7.88 (s, 2H), 6.88–7.01 (m, 4H), 3.21 (s, 3H), 3.03 (s, 4H), 2.71 (s, 4H), 2.54 (s, 4H); ^{13}C -NMR (100 MHz, DMSO- D_6) δ 172.7, 161.9, 152.6, 148.2, 136.5, 132.6, 125.3, 122.5, 121.2, 117.3, 115.6, 53.2, 52.8, 49.7, 44.0, 33.3; LC-MS: m/z ; 463 ($M + 1$); anal. calcd for: $C_{21}H_{23}FN_4O_3S_2$; C, 54.53; H, 5.01; N, 12.11; found: C, 54.31; H, 5.19; N, 12.39.



4.4.3. 3-[4-(4-Chloro-phenyl)-piperazin-1-yl]-N-(6-methanesulfonyl-benzothiazol-2-yl)-propionamide (6). White solid; yield 75% (204.0 mg); mp 210–212 °C. ¹H-NMR (400 MHz, DMSO-D6) δ 8.59 (s, 1H), 7.89 (s, 2H), 7.17 (d, *J* = 8.7 Hz, 2H), 6.89 (d, *J* = 8.7 Hz, 2H), 3.21 (s, 3H), 3.08 (s, 4H), 2.71 (s, 4H), 2.53 (s, 4H); ¹³C-NMR (100 MHz, DMSO-D6) δ 172.2, 162.3, 152.6, 150.2, 135.9, 132.4, 128.9, 125.3, 122.8, 122.6, 121.3, 117.3, 53.5, 52.7, 48.5, 44.4, 33.3; δ LC-MS: *m/z*; 480 (M + 1); anal. calcd for: C₂₁H₂₃ClN₄O₃S₂; C, 52.65; H, 4.84; N, 11.70; found: C, 52.44; H, 5.07; N, 11.98.

4.4.4. N-(6-Methanesulfonyl-benzothiazol-2-yl)-3-[4-(4-nitro-phenyl)-piperazin-1-yl]-propionamide (7). White solid; yield 82% (212.7 mg); mp 209–211 °C. ¹H-NMR (400 MHz, DMSO-D6) δ 8.59 (s, 1H), 8.00 (d, *J* = 9.2 Hz, 2H), 7.89 (s, 2H), 6.99 (d, *J* = 9.2 Hz, 2H), 3.41 (s, 4H), 3.21 (s, 3H), 2.71 (s, 4H), 2.52 (s, 4H); ¹³C-NMR (100 MHz, DMSO-D6) δ 172.3, 162.4, 155.2, 152.5, 137.3, 135.5, 132.5, 126.2, 125.4, 123.1, 122.6, 121.1, 113.1, 53.5, 52.2, 46.7, 44.5, 33.5; LC-MS: *m/z*; 490 (M + 1); anal. calcd for: C₂₁H₂₃N₅O₅S₂; C, 51.52; H, 4.74; N, 14.31; found: C, 51.29; H, 4.55; N, 14.58.

4.4.5. N-(6-Methanesulfonyl-benzothiazol-2-yl)-3-(4-*p*-tolyl-piperazin-1-yl)-propionamide (8). White solid; yield 84% (224.1 mg); mp 197–198 °C. ¹H-NMR (400 MHz, DMSO-D6) δ 8.59 (s, 1H), 7.89 (s, 2H), 6.97 (d, *J* = 8.2 Hz, 2H), 6.78 (d, *J* = 8.2 Hz, 2H), 3.21 (s, 3H), 3.02 (s, 4H), 2.71 (s, 4H), 2.54 (s, 4H), 2.15 (s, 3H); ¹³C-NMR (100 MHz, DMSO-D6) δ 172.4, 161.7, 152.3, 149.2, 136.3, 132.6, 130.2, 127.9, 125.0, 122.8, 121.6, 115.8, 53.8, 52.6, 49.1, 44.6, 32.9, 20.4; LC-MS: *m/z*; 459 (M + 1); anal. calcd for: C₂₂H₂₆N₄O₃S₂; C, 57.62; H, 5.71; N, 12.22; found: C, 57.37; H, 5.94; N, 12.02.

4.4.6. N-(6-Methanesulfonyl-benzothiazol-2-yl)-3-[4-(4-methoxy-phenyl)-piperazin-1-yl]-propionamide (9). White solid; yield 79% (202.8 mg); mp 177–179 °C. ¹H-NMR (400 MHz, DMSO-D6) δ 8.59 (s, 1H), 7.89 (s, 2H), 6.83 (d, *J* = 9.2 Hz, 2H), 6.76 (d, *J* = 9.2 Hz, 2H), 3.63 (s, 3H), 3.21 (s, 3H), 2.96 (d, *J* = 4.1 Hz, 4H), 2.71 (s, 4H), 2.54 (t, *J* = 4.1 Hz, 4H); ¹³C-NMR (100 MHz, DMSO-D6) δ 172.1, 162.3, 152.9, 152.3, 149.1, 145.8, 135.8, 131.9, 130.8, 127.8, 124.8, 120.5, 117.0, 114.4, 55.6, 53.5, 52.9, 50.1, 44.5, 33.3; LC-MS: *m/z*; 475 (M + 1); anal. calcd for: C₂₂H₂₆N₄O₄S₂; C, 55.68; H, 5.52; N, 11.81; found: C, 55.44; H, 5.71; N, 11.60.

4.4.7. 3-(4-Benzyl-piperazin-1-yl)-N-(6-methanesulfonyl-benzothiazol-2-yl)-propionamide (10). White solid; yield 76% (207.9 mg); mp 147–149 °C. ¹H-NMR (400 MHz, DMSO-D6) δ 8.59 (s, 1H), 7.89 (s, 2H), 7.24 (dt, *J* = 23.5, 7.2 Hz, 5H), 3.40 (s, 2H), 3.21 (s, 3H), 2.65 (s, 4H), 2.34–2.46 (m, 8H); ¹³C-NMR (100 MHz, DMSO-D6) δ 172.5, 162.6, 152.3, 140.4, 138.9, 135.6, 132.6, 128.6, 127.3, 125.5, 122.7, 121.4, 62.5, 53.0, 52.8, 44.5, 33.3; LC-MS: *m/z*; 459 (M + 1); anal. calcd for: C₂₂H₂₆N₄O₃S₂; C, 57.62; H, 5.71; N, 12.22; found: C, 57.81; H, 5.49; N, 12.48.

4.4.8. 3-(4-Benzhydryl-piperazin-1-yl)-N-(6-methanesulfonyl-benzothiazol-2-yl)-propionamide (11). White solid; yield 88% (216.8 mg); mp 170–172 °C. ¹H-NMR (400 MHz, DMSO-D6) δ 8.59 (s, 1H), 7.89 (s, 2H), 7.37 (d, *J* = 7.8 Hz, 4H), 7.24 (t, *J* = 7.6 Hz, 4H), 7.13 (t, *J* = 7.3 Hz, 2H), 4.21 (s, 1H), 3.21 (s, 3H), 2.64 (s, 4H), 2.26–2.46 (m, 8H); LC-MS: *m/z*; 535 (M + 1); anal. calcd for:

C₂₈H₃₀N₄O₃S₂; C, 62.90; H, 5.66; N, 10.48; found: C, 63.12; H, 5.89; N, 10.23.

4.4.9. N-(6-Methanesulfonyl-benzothiazol-2-yl)-3-(4-pyridin-2-yl-piperazin-1-yl)-propionamide (12). White solid; yield 74% (199.8 mg); mp 201–203 °C. ¹H-NMR (400 MHz, DMSO-D6) δ 8.59 (s, 1H), 8.05 (s, 1H), 7.89 (s, 2H), 7.47 (t, *J* = 7.6 Hz, 1H), 6.77 (d, *J* = 8.7 Hz, 1H), 6.58 (t, *J* = 6.0 Hz, 1H), 3.42 (s, 4H), 3.21 (s, 3H), 2.71 (s, 4H), 2.48 (s, 4H); ¹³C-NMR (100 MHz, DMSO-D6) δ 172.5, 162.3, 159.2, 152.6, 147.9, 138.0, 136.0, 132.5, 125.3, 122.5, 121.3, 113.5, 107.6, 53.6, 52.7, 45.1, 44.5, 33.4; LC-MS: *m/z*; 446 (M + 1); anal. calcd for: C₂₀H₂₃N₅O₃S₂; C, 53.91; H, 5.20; N, 15.72; found: C, 53.91; H, 5.20; N, 15.72; found: C, 53.69; H, 5.02; N, 15.95.

4.4.10. N-(6-Methanesulfonyl-benzothiazol-2-yl)-3-(4-pyrimidin-2-yl-piperazin-1-yl)-propionamide (13). White solid; yield 81% (204.2 mg); mp 174–176 °C. ¹H-NMR (400 MHz, DMSO-D6) δ 12.21 (s, 1H), 8.59 (s, 1H), 8.30 (d, *J* = 4.7 Hz, 2H), 7.89 (s, 2H), 6.57 (t, *J* = 4.7 Hz, 1H), 3.66–3.68 (m, 4H), 3.21 (s, 3H), 2.70 (s, 4H), 2.45–2.47 (m, 4H); ¹³C-NMR (100 MHz, DMSO-D6) δ 172.3, 162.5, 161.7, 158.4, 152.5, 135.8, 132.5, 125.3, 122.5, 121.3, 110.6, 53.6, 52.7, 44.5, 43.6, 33.2; LC-MS: *m/z*; 447 (M + 1); anal. calcd for: C₁₉H₂₂N₆O₃S₂; C, 51.10; H, 4.97; N, 18.82; found: C, 50.85; H, 5.09; N, 18.55.

4.4.11. 3-[4-(Furan-2-carbonyl)-piperazin-1-yl]-N-(6-methanesulfonyl-benzothiazol-2-yl)-propionamide (14). White solid; yield 69% (156.8 mg); mp 190–192 °C. ¹H-NMR (400 MHz, DMSO-D6) δ 8.59 (s, 1H), 7.88 (s, 2H), 6.88–7.01 (m, 4H), 3.21 (s, 3H), 3.03 (s, 4H), 2.71 (s, 4H), 2.54 (s, 4H); ¹³C-NMR (100 MHz, DMSO-D6) δ 172.2, 162.5, 158.6, 152.5, 147.1, 145.2, 136.1, 132.4, 124.6, 122.8, 121.4, 115.9, 111.1, 53.4, 53.0, 44.5, 33.4; LC-MS: *m/z*; 463 (M+1); anal. calcd for: C₂₀H₂₂N₄O₅S₂; C, 51.93; H, 4.79; N, 12.11; found: C, 51.71; H, 4.99; N, 12.32.

4.4.12. 4-[2-(6-Methanesulfonyl-benzothiazol-2-yl carbamoyl)-ethyl]-piperazine-1-carboxylic acid benzyl ester (15). White solid; yield 86% (226.7 mg); mp 159–161 °C. ¹H-NMR (400 MHz, DMSO-D6) δ 8.59 (s, 1H), 7.89 (s, 2H), 7.29 (d, *J* = 17.4 Hz, 5H), 5.03 (s, 2H), 3.32 (d, 4H), 3.21 (s, 3H), 2.67 (s, 4H), 2.37 (s, 4H); ¹³C-NMR (100 MHz, DMSO-D6) δ 172.4, 162.4, 154.9, 152.2, 137.5, 135.7, 132.4, 128.8, 128.3, 127.9, 125.1, 122.5, 121.0, 66.7, 53.5, 52.6, 44.4, 43.9, 33.4; LC-MS: *m/z*; 503 (M + 1); anal. calcd for: C₂₃H₂₆N₄O₅S₂; C, 54.96; H, 5.21; N, 11.15; found: C, 55.20; H, 5.02; N, 11.32.

4.4.13. 3-(4-Benzo[1,3]dioxol-5-yl methyl-piperazin-1-yl)-N-(6-methanesulfonyl-benzothiazol-2-yl)-propionamide (16). White solid; yield 75% (201.4 mg); mp 206–208 °C. ¹H-NMR (400 MHz, DMSO-D6) δ 12.70 (s, 1H), 8.59 (s, 1H), 7.89 (s, 2H), 6.78 (d, *J* = 6.7 Hz, 2H), 6.68 (d, *J* = 8.9 Hz, 1H), 5.93 (s, 2H), 3.330 (s, 2H), 3.21 (s, 3H), 2.64 (s, 4H), 2.31–2.46 (m, 8H); ¹³C-NMR (100 MHz, DMSO-D6) δ 172.3, 162.2, 152.4, 143.4, 135.7, 132.4, 129.0, 128.0, 127.3, 125.2, 122.7, 121.2, 75.6, 53.5, 53.0, 51.9, 44.4, 33.3; LC-MS: *m/z*; 503 (M + 1); anal. calcd for: C₂₃H₂₆N₄O₅S₂; C, 54.96; H, 5.21; N, 11.15; found: C, 54.71; H, 4.99; N, 10.90.

4.4.14. N-(6-Methanesulfonyl-benzothiazol-2-yl)-3-[4-(4-trifluoromethyl-phenyl)-piperazin-1-yl]-propionamide (17). White solid; yield 71% (208.8 mg); mp 197–199 °C. ¹H-NMR (400 MHz, DMSO-D6) δ 8.62–8.54 (1H), 7.89 (s, 2H), 7.45 (d, *J* = 8.8 Hz, 2H), 7.02 (d, *J* = 8.8 Hz, 2H), 3.22 (dd, *J* = 9.6, 4.4 Hz, 7H), 2.71 (s, 4H), 2.53 (t, *J* = 4.8 Hz, 4H); ¹³C-NMR (100 MHz, DMSO-D6) δ 172.8, 161.9, 154.3, 152.3, 135.3, 132.8, 126.6, 124.8, 122.4, 121.2, 113.8;



LC-MS: m/z ; 513 ($M + 1$); anal. calcd for: $C_{22}H_{23}F_3N_4O_3S_2$; C, 51.55; H, 4.52; N, 10.93; found: C, 51.29; H, 4.28; N, 11.21.

4.5. Inhibition of AChE and BuChE by synthesized derivatives

To determine the compound's ability to inhibit AChE and BuChE revised Ellman methods were performed. Concisely, stock solution of test compounds (10 mM) were prepared in 100% DMSO and diluted using autoclaved water to attain a final concentration range between (0.01–100) μM . Six different range of drug concentration was used to perform the assay. Enzyme dilutions and substrate dilutions were prepared according to the protocol. This assay was performed as reported by our lab previously.^{22,54}

4.6. Kinetic characterization of AChE inhibition by compound 12

To study the kinetics of AChE inhibition, three concentrations of compound 12 (2 μM , 6 μM and 8 μM) were selected. A reciprocal plot of $1/\text{velocity}$ versus $1/\text{substrate}$ was plotted at low substrate concentrations by using modified Ellman's method.⁵⁴

4.7. Inhibition of self-mediated $A\beta_{1-42}$ aggregation assay

Marketed amyloid beta peptides were obtained and dissolved in hexafluoroisopropanol (HFIP) at 8 mg ml^{-1} . The HFIP was evaporated and then $A\beta_{1-42}$ stocks were prepared in DMSO, finally diluted in reaction buffer (50 mM phosphate buffer (pH 7.4)). For the inhibition of self-mediated $A\beta_{1-42}$ aggregation experiment, ThT assay was performed as reported by our research group.²⁴

4.8. Disaggregation of self-induced $A\beta_{1-42}$ aggregation

For the study of disaggregation of self-induced $A\beta_{1-42}$ aggregation, peptide (100 μM) was incubated at 37 °C for 48 h to form amyloid beta fibrils and further the compounds were added and incubated again at 37 °C for 24 h. ThT method was used to quantify amyloid fibril formation.⁵⁴

4.9. Inhibition of self-mediated $A\beta_{1-42}$ aggregation by ThT assay using confocal microscopy

Peptide (10 μl) and compounds (10 μl) were incubated for 48 h at 37 °C. 5 μl from incubation mixture was diluted with 10 μM of ThT (1 : 2) *i.e.*, 10 μl of ThT in glycine–NaOH and placed on glass slide. Fluorescence signal of samples were analyzed at 488 nm by confocal laser scanning microscope.

4.10. Inhibition of self-mediated $A\beta_{1-42}$ aggregation using TEM

Solution of $A\beta$ stock was diluted with 50 mM phosphate buffer (pH 7.4), and further incubated in the presence and absence of compound 12 at 37 °C for 48 h. The final concentrations of $A\beta$ peptide and 12 were 50 μM , respectively. Aliquots (10 μl) of the samples were put on carbon-coated copper grid. Each grid was negatively stained with 0.5% phosphotungstate (PTA) solution

for 1 min at RT. Specimen was further transferred for imaging with transmission electron microscopy (JEOL JEM-1400).⁵⁵

4.11. Metal chelation studies

The ability of compounds to chelate metal ions was performed by UV-spectroscopy. Compound 12 (60 μM) was dissolved in HEPES buffer with and without the metal ions. UV absorption spectra were recorded with wavelength ranging from 200 to 600 nm. The stoichiometry of the complex 12– Cu^{2+} was determined by Job's method. The tested compound and copper ion were incubated at different molar ratios and UV absorption was plotted.⁵⁵

4.12. Molecular docking studies

Atomic coordinates of AChE (PDB ID: 1EVE) and $A\beta_{1-42}$ (PDB ID: 1YT) were taken from the Protein Data Bank (www.rcsb.org). Autodock 4.2 with standard protocol was used to dock the synthesized compound 12 with AChE and $A\beta_{1-42}$.¹⁶ Protein–ligands interactions were assessed by applying Lamarckian genetic algorithm (LGA). The most encouraging free binding energy and docking orientations lying within the range of 2.0 Å in root-mean square deviation (RMSD) tolerance were used to cluster the molecule and ranked accordingly. PyMOL was employed to visualize molecular interactions. All calculations were carried out on workstation machines running Linux x86 as operating systems.⁵⁶

4.13. Molecular dynamic (MD) simulation studies

MD simulations were carried out with GROMACS 4.6.5 suite of programs, using charm force-field and spc216 water molecules. The trajectory files were analyzed using GROMACS utilities: *g_gyrate*, *g_rmsd* and *g_rmsf* to obtain the radius of gyration (R_g), root mean square deviation (RMSD) and root mean square fluctuation (RMSF). The coordinates of AChE and $A\beta_{1-42}$ were minimized with steepest descent, up to a tolerance of 100 kJ mol^{-1} to remove all bad contacts. Two independent MD simulations were carried out with standard protocol in water for AChE and AChE–12 complex, respectively at 300 K to evaluate the structural changes, binding affinity and stability in course of simulation. Similarly, another set of MD simulations were performed for $A\beta_{1-42}$ and $A\beta_{1-42}$ –12 complex. The SHAKE algorithm was used to restrain the covalent bonds containing hydrogen atoms at their equilibrium distances and periodic boundary conditions were applied. Particle Mesh Ewald (PME) method was employed for computing the long-range electrostatic interactions. A 1.4 nm cut-off for van der Waals interactions and a 1.0 nm cut-off for Coulombs interaction were adopted in the simulation, respectively. Analytical graphs were plotted using Xmgrace, VMD and PyMol were used for structure and molecular interaction analysis.^{22,53}

4.14. Cytotoxicity of synthetic compounds on SHSY-5Y cell line

To study the cytotoxicity of the compound 12 on neuronal cells, MTT assay was performed. 1×10^4 cells per well were seeded in



96-well plates. The medium was removed after 24 h and compound **12** at different concentrations (5 μM , 10 μM and 20 μM) for 24 h at 37 $^{\circ}\text{C}$ were added. After 24 h, MTT (5 mg ml^{-1} stock) solution (20 μl) per well were added at 37 $^{\circ}\text{C}$ for 4 h. MTT was removed thereafter and formazon crystals were then dissolved in DMSO. The absorbance at 570 nm was recorded. Results have been shown as the mean \pm SD of three independent experiments.²²

4.15. Neuroprotection against H_2O_2 induced neurotoxicity

To study the neuroprotective effects of the compound against hydrogen peroxide (H_2O_2) induced neurotoxicity, MTT assay was performed. 2×10^4 per well SH-SY5Y cells were seeded in 96-well plates. Serum free medium was added after 24 h of incubation, containing different concentrations of the compounds **12** followed by 200 μM H_2O_2 after an interval of 3 hours at 37 $^{\circ}\text{C}$ for 24 h. Cells without treatment were used as healthy controls and cells treated with H_2O_2 as control group were used and the results were evaluated as percentage of control. Photomicrographs were also captured using camera attached to the microscope (Olympus, Japan) after 24 h of treatment to assess morphological changes in SH-SY5Y cells.²⁴

4.16. Animals

Swiss albino male mice (25–30 g, 2–3 weeks; $n = 6$ each group) was procured from animal house facility of Dr. B. R. Ambedkar Center for Biomedical Research, University of Delhi, Delhi, India. Polypropylene cages were used for housing the animals and optimum conditions (temperature 25 ± 2 $^{\circ}\text{C}$, 12 h light/12 h dark cycle, $50 \pm 5\%$ relative humidity and free access to food and water *ad libitum*) were maintained under the standard laboratory environmental conditions. Thus, all animal procedures were performed in accordance with the guidelines for care and use of laboratory animals of Institutional Animal Ethics Committee (IAEC), Dr. B.R. Ambedkar Center for Biomedical Research, Delhi University and approved by the animal ethics Committee for the Purpose of Control and Supervision of Experiments on Animals (CPCSEA), Government of India.

4.17. Drugs and experimental design

Scopolamine hydrobromide was procured from Sigma-Aldrich (MO, USA). Scopolamine was dissolved in saline and given intraperitoneally (i.p.) in a dose of 3 mg kg^{-1} . Five groups with $n = 6$ were designed and mice were randomly allocated in each group. Animals in group I were given scopolamine 3 mg kg^{-1} b. wt per day, i.p.^{51,52}. Group II animals were treated together with scopolamine 3 mg kg^{-1} b. wt per day, i.p. and standard drug Donepezil (5 mg kg^{-1} b. wt per day; i.p.). In groups III & IV, scopolamine followed by treatment with compound **12** (10 and 20 mg kg^{-1} b. wt per day, i.p.) were given. Animals in group V were used as vehicle controls and they were administered saline (daily, i.p.). For 7 consecutive days, all the drugs including scopolamine were given daily. Behavioural studies were carried out, at the end of treatment schedules. Elevated plus maze

(EPM) task and social recognition test were performed for each animal in each group.

4.18. Elevated plus maze test (EPM)

There are two open arms (50 cm \times 10 cm) and two closed arms (50 cm \times 10 cm \times 30 cm) in the elevated plus maze. There is a central platform elevated to a height of 50 cm from the floor. The experiments were performed in the light phase. At one edge of the arm, we placed the mice facing the opposite side and recorded the time taken by animals to enter the closed arm which was documented as transfer of latency (T_1).⁵²

4.19. Social recognition test

The behavioural assay was performed according to the protocol given by Timmermann *et al.*⁵⁷ The adult mice and the juvenile (8–12 g) were kept together to make acquainted to themselves, for 1 h in the test room. Thereafter, the adult mice were brought back to their respective cages. The first interactive trial (T_1) of the adult mice with the juvenile mice began after 30 min of habituation period. The adult mice were placed with the juvenile and the interaction time (T_1) was recorded and observed simultaneously for 5 min. This was subsequently repeated for all the groups. The second trial began after 120 min in the same test cage pursued by recording the time in seconds of adult mice interacting with the juvenile mice. The obtained results were given in the form of recognition ratios (T_2/T_1). Index of improved short term recognition memory is the decrease in $T_2 : T_1$.

Conflicts of interest

There are no conflicts to declare.

Acknowledgements

Author C. B. M would like to acknowledge the financial support from DHR for Young Scientist fellowship. Author S. S is thankful to Ministry of AYUSH for the financial support (JRF). M. T wishes to acknowledge University of Delhi, UGC-SAP and DST-PURSE for providing research funds to carry out the study. The authors gratefully acknowledge animal facility of ACBR and NMR facility of USIC and TEM facility of SAIF, AIIMS.

References

- 1 M. Citron, *Nat. Neurosci.*, 2002, 5, 1055–1057.
- 2 B. Klimova, P. Maresova and K. Kuca, *Curr. Alzheimer Res.*, 2016, 13, 1249–1258.
- 3 P. Marešová, H. Mohelská, J. Dolejš and K. Kuča, *Curr. Alzheimer Res.*, 2015, 12, 903–911.
- 4 H. C. Beerens, C. Sutcliffe, A. Renom-Guiteras, M. E. Soto, R. Suhonen, A. Zabalegui, C. Bökberg, K. Saks and J. P. Hamers, *J. Am. Med. Dir. Assoc.*, 2014, 15, 54–61.
- 5 C. Haass and D. J. Selkoe, *Nat. Rev. Mol. Cell Biol.*, 2007, 8, 101–112.



- 6 T. P. Knowles, M. Vendruscolo and C. M. Dobson, *Nat. Rev. Mol. Cell Biol.*, 2014, **15**, 384–396.
- 7 S. Ayala, P. Genevaux, C. Hureau and P. Faller, *ACS Chem. Neurosci.*, 2019, **10**, 3366–3374.
- 8 C. Cheignon, M. Tomas, D. Bonnefont-Rousselot, P. Faller, C. Hureau and F. Collin, *Redox Biol.*, 2018, **14**, 450–464.
- 9 G. Nesi, S. Sestito, M. Digiacoimo and S. Rapposelli, *Curr. Top. Med. Chem.*, 2017, **17**(27), 3062–3079.
- 10 C. Cheignon, M. Tomas, D. Bonnefont-Rousselot, P. Faller, C. Hureau and F. Collin, *Redox Biol.*, 2018, **14**, 450–464.
- 11 G. Caruso, S. F. Spampinato, V. Cardaci, F. Caraci, M. A. Sortino and S. Merlo, *Curr. Pharm. Des.*, 2019, **25**(45), 4771–4781.
- 12 K. A. Jellinger, *J. Cell. Mol. Med.*, 2010, **14**, 457–487.
- 13 A. I. Bush, *J. Alzheimer's Dis.*, 2013, **33**, S277–S281.
- 14 M. L. Seux, J. Rotrou and A. S. Rigaud, *PSN*, 2008, **6**, 82–90.
- 15 K. Blennow, M. J. de Leon and H. Zetterberg, *Lancet*, 2006, **368**, 387–403.
- 16 K. G. Yiannopoulou and S. G. Papageorgiou, *Ther. Adv. Neurol. Disord.*, 2013, **6**, 19–33.
- 17 R. Anand, K. D. Gill and A. A. Mahdi, *Neuropharmacology*, 2014, **76**, 27–50.
- 18 R. Ali, I. A. Sheikh, N. R. Jabir and M. A. Kamal, *Am. J. Neuroprot. Neuroregener.*, 2012, **4**, 136–144.
- 19 S. Sestito, S. Wang, Q. Chen, *et al.*, *Eur. J. Med. Chem.*, 2019, **174**, 216–225.
- 20 M. Maspero, D. Volpato, D. Cirillo, *et al.*, *Bioorg. Chem.*, 2020, **96**, 103633.
- 21 F. J. Pérez-Areales, A. L. Turcu, M. Barniol-Xicota, *et al.*, *Eur. J. Med. Chem.*, 2019, **180**, 613–626.
- 22 C. B. Mishra, S. Kumari, A. Manral, A. Prakash, V. Saini, A. M Lynn and M. Tiwari, *Eur. J. Med. Chem.*, 2017, **125**, 736–750.
- 23 A. Manral, V. Saini, P. Meena and M. Tiwari, *Bioorg. Med. Chem.*, 2015, **23**, 6389–6403.
- 24 C. B. Mishra, A. Manral, S. Kumari, V. Saini and M. Tiwari, *Bioorg. Med. Chem.*, 2016, **24**, 3829–3841.
- 25 J. M. Song, A. M. Di Battista, Y. M. Sung, J. M. Ahn, R. S. Turner, J. Yang, D. T. Pak, H. K. Lee and H. S. Hoe, *Exp. Neurol.*, 2014, **252**, 105–113.
- 26 R. Ali and N. Siddiqui, *J. Chem.*, 2013, 1–12.
- 27 C. A. Mathis, N. S. Mason, B. J. Lopresti and W. E. Klunk, *Semin. Nucl. Med.*, 2012, **42**, 423–432.
- 28 C. B. Mishra, S. Kumari and M. Tiwari, *Eur. J. Med. Chem.*, 2015, **6**, 1–34.
- 29 N. Guziar, A. Wieckowska, D. Panek and B. Malawska, *Curr. Med. Chem.*, 2015, **22**(3), 373–404.
- 30 C. B. Mishra, S. Kumari, A. Angeli, S. M. Monti, M. Buonanno, M. Tiwari and C. T. Supuran, *J. Med. Chem.*, 2017, **60**, 2456–2469.
- 31 C. B. Mishra, S. Kumari, A. Angeli, S. Bua, M. Tiwari and C. T. Supuran, *J. Med. Chem.*, 2018, **61**, 3151–3165.
- 32 S. Kumari, C. B. Mishra and M. Tiwari, *Pharmacol. Rep.*, 2016, **68**, 250–258.
- 33 D. Özkay Ümide, C. Ö. Devrim, Y. Ozkay and Y. Ozturk, *Pharmacol. Rep.*, 2012, **64**, 834–847.
- 34 S. Stayte and B. Vissel, *Front. Neurosci.*, 2014, **8**, 113.
- 35 A. K. Rathi, R. Syed, H. S. Shin and R. V. Patel, *Expert Opin. Ther. Pat.*, 2016, **26**(7), 777–797.
- 36 L. Peauger, R. Azzouz, V. Gembus, M. L. Țințaș, J. S. O. Sopková-de, P. Bohn, C. Papamicaël and V. Levacher, *J. Med. Chem.*, 2017, **60**, 5909–5926.
- 37 G. L. Ellman, K. D. Courtney, V. Andres Jr and R. M. Featherstone, *Biochem. Pharmacol.*, 1961, **7**, 88–95.
- 38 D. R. Liston, *et al.*, Pharmacology of selective acetylcholinesterase inhibitors: implications for use in Alzheimer's disease, *Eur. J. Pharmacol.*, 2004, **486**, 9–17.
- 39 Li Luo, *et al.*, Design, synthesis and evaluation of phthalide alkyl tertiary amine derivatives as promising acetylcholinesterase inhibitors with high potency and selectivity against Alzheimer's disease, *Bioorg. Med. Chem.*, 2020, 115400.
- 40 A. Kumar, A. Singh and Ekavali, *Pharmacol. Rep.*, 2015, **67**(2), 195–203, DOI: 10.1016/j.pharep.2014.09.004.
- 41 H. Aoyama and T. Doura, *Bioorg. Med. Chem. Lett.*, 2020, **30**, 126888.
- 42 G. A. de Souza, *et al.*, *J. Enzyme Inhib. Med. Chem.*, 2019, **34**, 631–637.
- 43 N. A. Vyas, S. B. Singh, A. S. Kumbhar, D. S. Ranade, G. R. Walke, P. P. Kulkarni, V. Jani, U. B. Sonavane, R. R. Joshi and S. Rapole, *Inorg. Chem.*, 2018, **57**, 7524–7535.
- 44 J. Hardy and D. J. Selkoe, *Science*, 2002, **297**, 353–356.
- 45 H. Du, X. Liu, J. Xie and F. Ma, *ACS Chem. Neurosci.*, 2019, **10**, 2397–2407.
- 46 O. Crescenzi, S. Tomaselli, R. Guerrini, S. Salvadori, A. M. D'Urso, P. A. Temussi and D. Picone, *Eur. J. Biochem.*, 2002, **269**, 5642–5648.
- 47 S. Vilasi, R. Carrotta, C. Ricci, G. C. Rappa, F. Librizzi, V. Martorana and M. R. Mangione, *ACS Chem. Neurosci.*, 2019, **10**(8), 3565–3574.
- 48 A. Prakash, G. Dixit, N. K. Meena, R. Singh, P. Vishwakarma, S. Mishra and A. M. Lynn, *J. Biomol. Struct. Dyn.*, 2018, **36**(9), 2391–2406.
- 49 L. Vugmeyster, M. A. Clark, I. B. Falconer, D. Ostrovsky, D. Gantz, W. Qiang and G. L. Hoatson, *J. Biol. Chem.*, 2016, **291**(35), 18484–18495.
- 50 J. Hardy and D. J. Selkoe, *Science*, 2002, **297**, 353–356.
- 51 A. Blokland, *Scopolamine Rev.*, 2005, **1**, 1–76.
- 52 A. C. Sharma and S. K. Kulkarni, *Prog. Neuro-Psychopharmacol. Biol. Psychiatry*, 1992, **16**, 117–125.
- 53 C. B. Mishra, S. Kumari, A. Prakash, R. Yadav, A. K. Tiwari, P. Pandey and M. Tiwari, *Eur. J. Med. Chem.*, 2018, **151**, 520–532.
- 54 T. Umar, S. Shalini, M. K. Raza, S. Gusain, J. Kumar, P. Seth, M. Tiwari and N. Hoda, *Eur. J. Med. Chem.*, 2019, **175**, 2–19.
- 55 T. Umar, S. Shalini, M. K. Raza, S. Gusain, J. Kumar, W. Ahmed, M. Tiwari and N. Hoda, *MedChemComm*, 2018, **9**, 1891–1904.
- 56 A. C. Wallace, R. A. Laskowski and J. M. Thornton, *Protein Eng. Des. Sel.*, 1995, **8**(2), 127–134.
- 57 D. B. Timmermann, K. Sandager-Nielsen, T. Dyhring, M. Smith, A. M. Jacobsen, E. Ø. Nielsen, M. Grunnet, J. K. Christensen, D. Peters, K. Kohlhaas, G. M. Olsen and P. K. Ahring, *Br. J. Pharmacol.*, 2012, **167**, 164–182.

